Provenance analysis using Raman spectroscopy of carbonaceous material: A case study in the Southern Alps of New Zealand

Lukas Nibourel, Frédéric Herman, Simon Cox, Olivier Beyssac, Jérôme Lavé

AGU PUBLICATIONS

JGR

Journal of Geophysical Research: Earth Surface

RESEARCH ARTICLE
10.1002/2015JF003541

Key Points:
- Raman Spectroscopy on CM can be used to perform provenance analysis
- When mapping sediment provenance, tracer concentration within bedrock needs to be considered
- Detrital sands record short-term (contemporary) uplift rather than long-term exhumation

Correspondence to:
L. Nibourel,
lukas.nibourel@geo.unibe.ch

Citation:
Nibourel, L., F. Herman, S. C. Cox, O. Beyssac, and J. Lavé (2015), Provenance analysis using Raman Spectroscopy of Carbonaceous Material: A case study in the Southern Alps of New Zealand, *J. Geophys. Res. Earth Surf.*, *120*, 2056–2079, doi:10.1002/2015JF003541.

Received 16 MAR 2015
Accepted 5 AUG 2015
Accepted article online 10 AUG 2015
Published online 15 OCT 2015

Provenance analysis using Raman spectroscopy of carbonaceous material: A case study in the Southern Alps of New Zealand

Lukas Nibourel[1,2], Frédéric Herman[1,3], Simon C. Cox[4], Olivier Beyssac[5], and Jérôme Lavé[6]

[1]Department of Earth Sciences, Federal Institute of Technology Zurich, Zurich, Switzerland, [2]Institute of Geological Sciences, University of Bern, Bern, Switzerland, [3]Institute of Earth Surface Dynamics, University of Lausanne, Lausanne, Switzerland, [4]GNS Science, Dunedin, New Zealand, [5]Institut de Minéralogie, de Physique des Matériaux, et de Cosmochimie, UMR CNRS 7590, Sorbonne Universités UPMC, Muséum National d'Histoire Naturelle, IRD, Paris, France, [6]Centre de Recherches Pétrographiques et Géochimiques (CRPG), CNRS-Université de Lorraine, France

Abstract Detrital provenance analyses in orogenic settings, in which sediments are collected at the outlet of a catchment, have become an important tool to estimate how erosion varies in space and time. Here we present how Raman Spectroscopy on Carbonaceous Material (RSCM) can be used for provenance analysis. RSCM provides an estimate of the peak temperature (RSCM-*T*) experienced during metamorphism. We show that we can infer modern erosion patterns in a catchment by combining new measurements on detrital sands with previously acquired bedrock data. We focus on the Whataroa catchment in the Southern Alps of New Zealand and exploit the metamorphic gradient that runs parallel to the main drainage direction. To account for potential sampling biases, we also quantify abrasion properties using flume experiments and measure the total organic carbon content in the bedrock that produced the collected sands. Finally, we integrate these parameters into a mass-conservative model. Our results first demonstrate that RSCM-*T* can be used for detrital studies. Second, we find that spatial variations in tracer concentration and erosion have a first-order control on the RSCM-*T* distributions, even though our flume experiments reveal that weak lithologies produce substantially more fine particles than do more durable lithologies. This result implies that sand specimens are good proxies for mapping spatial variations in erosion when the bedrock concentration of the target mineral is quantified. The modeling suggests that highest present-day erosion rates (in Whataroa catchment) are not situated at the range front but around 10 km into the mountain belt.

1. Introduction

Quantifying catchment-scale erosion in mountain belts is key to understanding landscape evolution. To that end, provenance studies of minerals contained in detrital sands are used to infer spatial patterns of erosion. For example, high-resolution petrographic analysis has been used successfully to assess the abundance and provenance of detrital minerals [e.g., *Ludwig*, 1874; *Dickinson*, 1988; *Garzanti and Vezzoli*, 2003] and infer erosion patterns in orogenic settings [e.g., *Garzanti et al.*, 2007]. Similarly, low-temperature thermochronology has been used to quantify basin-averaged erosion rate, or map sediment source areas, by comparing the distribution of cooling ages observed in sand specimens to the spatial distribution of bedrock cooling ages within a catchment [e.g., *Stock et al.*, 2006; *Huntington and Hodges*, 2006; *McPhillips and Brandon*, 2010; *Malusà et al.*, 2009]. Likewise, radiogenic isotopes measured in river and marine sediments have been shown useful as source tracers [e.g., *Galy and France-Lanord*, 2001; *Pierson-Wickmann et al.*, 2002; *Galy et al.*, 2010]. However, these isotope techniques usually yield a relatively coarse spatial resolution on sediment provenance, because they primarily rely on age contrasts in the source rocks. Therefore, such tracers may often not be very sensitive in small mountain catchments for studies that wish to gain insight on small-scale spatial patterns of erosion.

Whether sediments collected at the basin outlet are representative of catchment erosion is rarely demonstrated and cannot necessarily be assumed. Transport can be complex and may introduce several sources of bias to assessments of provenance. Among potential sources of bias, the in situ bedrock concentration of a target mineral tracer modulates the sampled distribution through preferential sampling of an area [e.g., *Moecher and Samson*, 2006; *Dickinson*, 2008; *Malusà et al.*, 2009]. In some settings, bias might be introduced

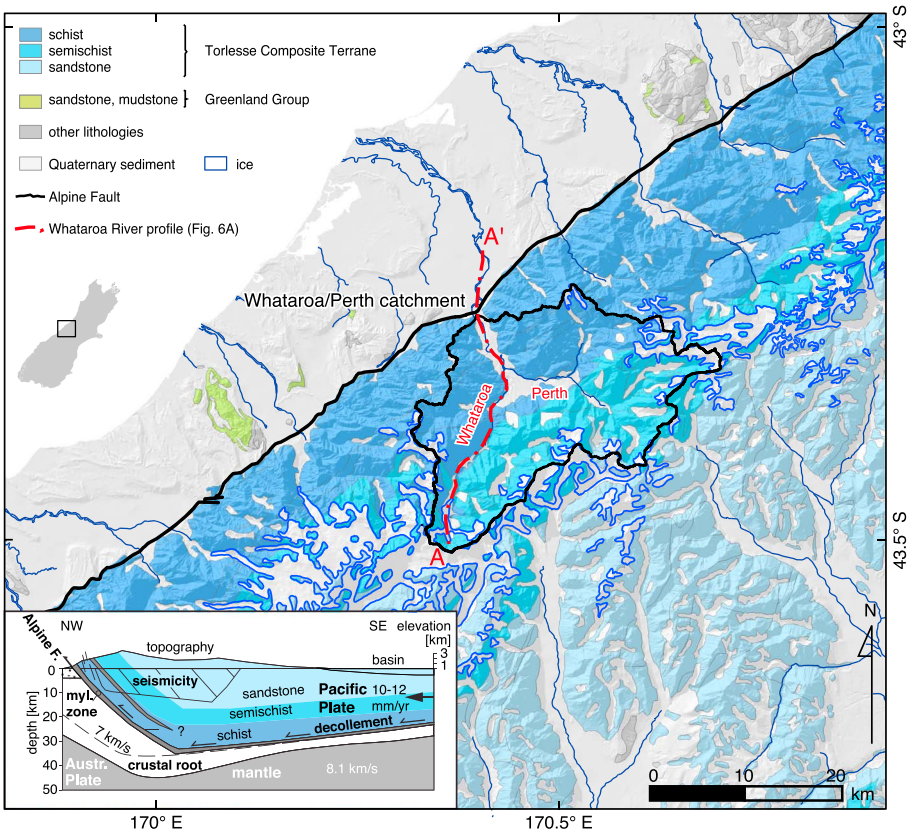

Figure 1. Modified geological map after *Cox and Barrell* [2007]. The hanging wall of the Alpine Fault is almost entirely composed of Carboniferous-Cretaceous Torlesse Composite Terrane sediment (blue), predominantly quartzofeldspathic greywacke sandstone with subordinate argillite, showing increased metamorphism toward the Alpine Fault. It is classified here on the degree of metamorphic textural reconstitution. The Greenland Group (green) on the Alpine Fault's footwall consists of sandstones and mudstones in flysch sequences that are superficially similar to the Torlesse Composite Terrane sandstone but are more quartz rich [*Cox and Barrell*, 2007]. For orientation, the location of the Whataroa catchment polygon (black polygon) and River profile (red dashed line, see also Figure 6a) are indicated on the map. A schematic cross section through the central Southern Alps, showing selected tectonic and geophysical features can be seen in the lower left corner (modified after *Little et al.* [2002], *Stern et al.* [2001], *Little et al.* [2005]). The profile is schematically colored according to the three main rock types in the hanging wall of the Alpine Fault: schist, semischist, and sandstone.

where there is geochemical and/or mineralogical fractionation of bed load and suspended load during transport [*Bouchez et al.*, 2011]. Some bias might also be induced because bed load evolves during fluvial transport [e.g., *Sternberg*, 1875; *Bradley*, 1970; *Parker*, 1991; *Attal and Lavé*, 2009], a process that depends on abrasion, which is a function of lithology, texture, grain size, and shape of sediment supplied to the river system and the hydrodynamic conditions [e.g., *Kuenen*, 1956; *Attal and Lavé*, 2009]. Consequently, if one wishes to quantify catchment erosion from sand-grade clastic sediments, it is preferable to have a good understanding of the physical disaggregation of rocks during fluvial transport.

The Southern Alps of New Zealand exhibit a range of unique features that are useful for erosion studies and, in particular, test new approaches. Here we focus on the Whataroa catchment located in the central Southern Alps. First, extremely high precipitation (6–10 m yr^{-1}) and uplift rates (~6–9 mm yr^{-1}) lead to high erosion and transport rates [e.g., *Whitehouse*, 1987; *Herman and Braun*, 2006; *Cox and Barrell*, 2007; *Herman et al.*, 2009, 2010]. Second, a well-constrained metamorphic gradient is observed in the hanging wall of the Alpine Fault [e.g., *Little et al.*, 2005], the main plate boundary fault of the orogen, and runs parallel to the main drainage direction (Figure 1). Third, O. Beyssac et al. (Thermal structure in schist exhumed along the Alpine Fault boundary, South Island, New Zealand, submitted to *Tectonophysics*, 2015) recently used Raman Spectroscopy on Carbonaceous Material (RSCM-*T*) on in situ bedrock of 140 sample points. During diagenesis and metamorphism, carbonaceous material of sedimentary origin is progressively transformed

into graphite (i.e., graphitization). *Beyssac et al.* [2002] demonstrated that the degree of graphitization can be quantified by Raman spectroscopy and that it is a reliable indicator of the peak temperature conditions reached during metamorphism (RSCM-*T*). Theoretical background and some applications are extensively described in *Beyssac and Lazzeri* [2012]. Our idea here is that carbonaceous material is delivered to rivers when the host metamorphic rocks are exposed to erosion. This potentially offers a proxy to trace the provenance of river sediments.

In this study, we use a multidisciplinary approach to trace sediment source, combining thermometry based on RSCM with a transport model constrained by abrasion experiments. We test this new approach in the actively eroding Whataroa catchment on the western side of the Southern Alps, New Zealand. Our results show that RSCM may be able to resolve provenance on a 1–10 km scale due to its sensitivity to metamorphic gradients. The relative ease of data acquisition and treatment make RSCM a potentially powerful tool for statistical provenance analysis. Finally, our results show that spatial variations of tracer concentration in situ bedrock and erosion have a first-order control on the provenance of detrital sands. Effects of bed load modifications during transport are small in the field, although large differences in terms of sand production are observed in the laboratory.

2. Setting

The Southern Alps of New Zealand are the result of the continental collision between the Australian and Pacific plates (*Cox and Sutherland* [2007] for a review). In the vicinity of the Whataroa catchment, the Southern Alps are rapidly uplifting with exhumation rates up to 9 mm yr^{-1} [*Batt et al.*, 2000; *Little et al.*, 2005; *Herman et al.*, 2007, 2009, 2010] within a 20–25 km wide zone southeast of the Alpine Fault [*Herman et al.*, 2009]. This major oblique-slip fault strikes northeast and dips 30–50° to the southeast, probably connecting at lower crustal levels to a shallow-easterly dipping decollement [*Kleffmann et al.*, 1998; *Norris and Cooper*, 1995; *Herman et al.*, 2009]. Rocks east of the Alpine Fault belong to the Torlesse Composite Terrane (Figure 1) a thick package of indurated Carboniferous-Cretaceous quartzofeldspathic sedimentary rocks that were metamorphosed during the Jurassic-Cretaceous, then overprinted by metamorphism and structurally reorganized during the Neogene. Fossil organic carbon is widespread in rocks of the Southern Alps, generally dispersed in the mineral matrix [*Hilton et al.*, 2008; O. Beyssac et al., submitted manuscript, 2015]. The RSCM technique takes advantage of the widespread occurrence of carbonaceous material.

A prominent metamorphic gradient is observed in the hanging wall of the Alpine Fault, going from amphibolite facies schist adjacent to the Alpine Fault, through greenschist facies schist and semischist, to uncleaved prehnite-pumpellyite facies greywacke sandstone (with minor argillite) toward the southeast (Figure 2) [*Little et al.*, 2005; *Cox et al.*, 2012; *Sibson et al.*, 1981]. In this paper we subdivide the degree of metamorphism of these rocks by both, index minerals and facies (metamorphic zones), and three simplified textural categories (textural zones) reflecting their physical strength properties [*Turnbull et al.*, 2001]: sandstone (uncleaved or weakly cleaved), semischist (cleaved and weakly foliated), and schist (weakly to strongly foliated), as shown in Figure 1. This dual metamorphic/textural classification is widely used by New Zealand geologists and is necessary to map variations of temperature and physical properties throughout the catchment. O. Beyssac et al. (submitted manuscript, 2015) acquired RSCM-*T* data for in situ bedrock across the entire Southern Alps. They reveal mean temperatures reaching more than 640°C close to the Alpine Fault decreasing down to values of less than 330°C in sandstone (Figure 2). For each bedrock thin section, 1 to 16 spectra were collected and automatically fitted using the method described in section 3.3. From this data set, we now extract the distribution of peak temperature for each metamorphic zone, combining all of the spectra collected in samples from each zone into a single histogram for that zone (Figure 3). Rather than using the entire data set, which spans a 300 km length of the Southern Alps, we only use samples located in the central Southern Alps. In turn, we observe a narrow distribution in high-grade metamorphic rocks that becomes significantly broader for lower-grade conditions. The width of the low-grade metamorphic zones reflects the presence of some detrital graphite in these rocks, as discussed below. Recycling of graphite has been observed in modern sedimentary environments [*Galy et al.*, 2008; *Bouchez et al.*, 2010], but it remains poorly constrained in the sedimentary archive so it is not possible to quantify its impact at present. We also show in Figure 3 the distribution of RSCM-*T* according to the textural classification based on development of metamorphic fabric.

Each distribution has been approximated by a normal probability density function (PDF, Figure 3). The quality of fit is assessed using a standard one-dimensional Kolmogorov-Smirnov test [see *Massey*, 1951] which

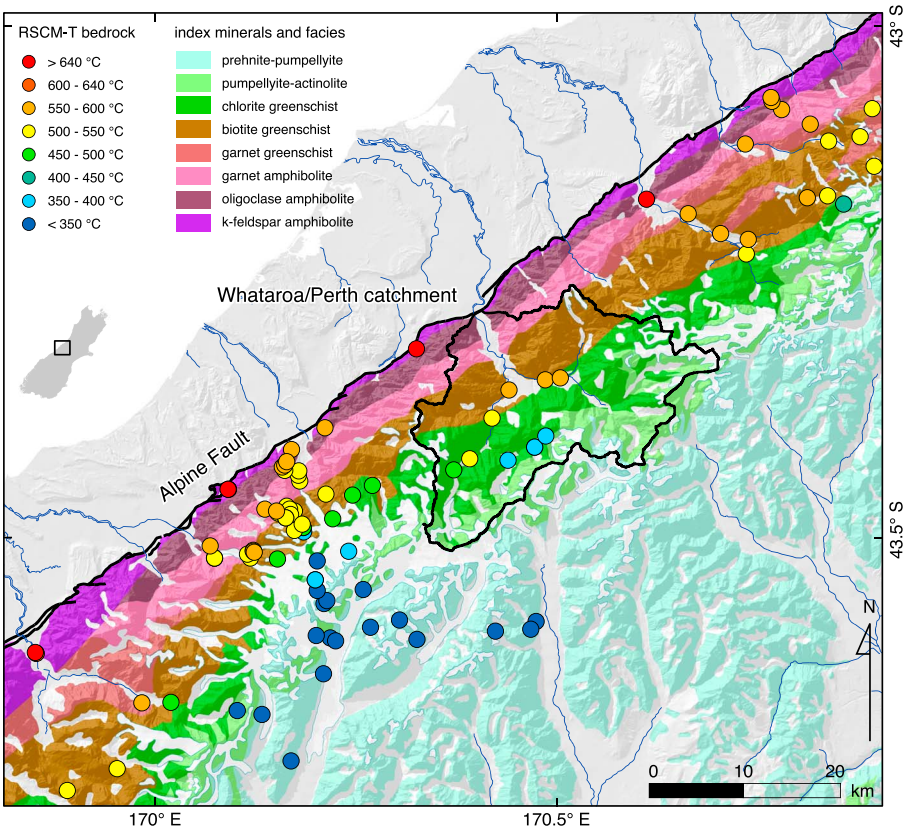

Figure 2. Index minerals and facies (metamorphic zones) of the central Southern Alps [*Cox and Barrell*, 2007]. Data points of mean RSCM-*T*, measured in bedrock thin sections were collected by O. Beyssac et al. (submitted manuscript, 2015). The location of the Whataroa catchment (black polygon) is indicated on the map.

is described in more detail in section 5.2. A reasonable fit can be achieved for all high-grade metamorphic zones. Low-grade metamorphic zones have a bimodal or broad, weakly defined, temperature distribution. Based on these results, we arbitrarily selected two temperatures that define the boundaries between sandstone, semischist and schist ($T_{sst/ss}$ = 356°C and $T_{ss/sch}$ = 492°C), which we will use below.

Mean annual rainfall in the Whataroa catchment is high (6–10 m) including events that have reached 758 mm d^{-1} [*Woods et al.*, 2006]. Heavy rainfall episodes produce elevated runoff or flood-level flows approximately 2 to 3 times per month [*National Institute of Water and Atmospheric Sciences*, 2013]. The Whataroa catchment is drained by two main rivers, the Whataroa and Perth, and its geomorphology can be divided into three main zones [*Whitehouse*, 1987; *Herman and Braun*, 2006]: (1) In the most upstream regions, glacial cirques dominate a bedrock landscape that is draped with a thin cover of ice, talus, colluvium, till, and landslide deposits. (2) In the intermediate zone, there are bedrock gorges and the river cuts through cover dominated by alluvial and talus fan deposits, which also includes colluvium and till deposits. (3) In the lower reaches of the catchment, there are well-preserved terraces of fluvioglacial outwash and alluvial fans that have been uplifted and incised southeast of the Alpine Fault, and an outwash plain that broadens into a braided channel system northwest of the fault where material is being rapidly deposited on the downthrown side. Throughout the catchment, stream, and river channels are highly active, switching course and eroding their banks during periods of flood. Sedimentary input into channels from cover deposits is composed of predominantly angular material in the upper alpine reaches, both angular and rounded in the intermediate zone, and almost exclusively rounded cobbles and pebbles in the lower part of the catchment. Once material has entered the river and stream channels as bed load, the frequency of storm events suggests that it is being redistributed on a monthly or bimonthly basis. *Cox and Nibourel* [2015] provide a detailed assessment of bed load in nearby rivers of Westland, demonstrating a close relationship between bed load composition and mapped catchment geology in the Southern Alps, albeit with some variation from one catchment to the next.

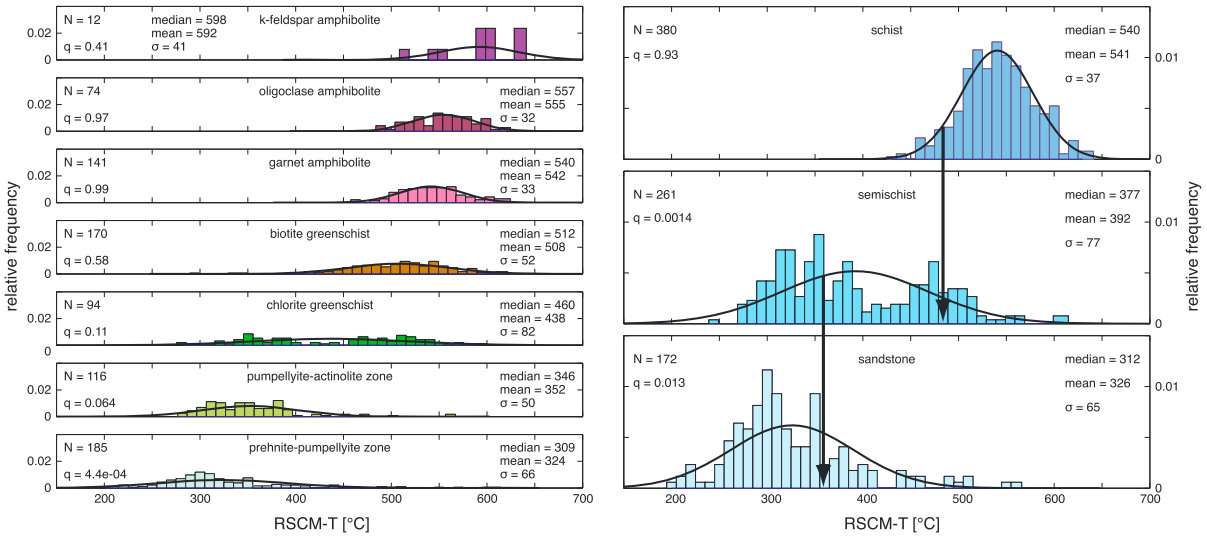

Figure 3. Histograms of RSCM-*T* bedrock field data plotted (left column) against metamorphic zones (also see Figure 2) and (right column) against metamorphic fabric development (also see Figure 1). The observed distributions of RSCM-*T* were approximated by a normal probability density function, which was plotted for each histogram (solid black line). Critical temperatures $T_{sst/ss} = 356°C$ and $T_{ss/sch} = 492°C$, were arbitrarily selected as a threshold to distinguish between adjacent textural zones (black arrows). *N* represents the number of fitted spectra. The *q* values estimate the goodness of fit between field data and Gaussian approximation. Data from O. Beyssac et al. (submitted manuscript, 2015).

Hilton et al. [2008] studied the composition of particulate organic carbon in suspension and bed load from various rivers in the Southern Alps, including the Whataroa. They have shown that the TOC (total organic carbon) and geochemical signature of carbon in bed load is highly similar to that of bedrock suggesting that carbon in sand size fraction of bed load is mostly, if not exclusively, derived from fossil organic carbon, while modern organic carbon is transported as suspended load. Transport of fossil organic carbon in sand size fraction of bed load was also evidenced in the Himalayan system [*Galy et al.*, 2008] and in the Amazon [*Bouchez et al.*, 2010]. In addition, the two latter studies demonstrated that there is no difference in terms of crystallinity patterns for graphitic carbon from the river surface to the bed material. *Galy et al.* [2008] observed selective oxidation of disordered fossil organic carbon and graphite preservation during transport in the large Indian rivers but not in mountainous settings that are associated with rapid sediment and short transport distances. In a small-scale and rapidly eroding system such as Taiwan, bearing many similarities with the Southern Alps of New Zealand, *Hilton et al.* [2014] concluded that physical erosion and export of fossil organic carbon in sediment represented 85–90% of the total mass flux of fossil organic carbon, with the remainder oxidized during chemical weathering in soils and colluvium. The oxidative loss was found to be linked to the physical erosion rate [*Hilton et al.*, 2014] and so it is likely to occur in the Southern Alps where erosion rates are high [*Herman et al.*, 2010]. This represents a potential bias if there is selective oxidation of fossil organic carbon subject to lower metamorphic temperatures being less mature and therefore more prone to oxidation [*Galy et al.*, 2008]. However, we note that other studies have reported such bias is likely to be minor in soils [*Petsch et al.*, 2000] and that fossil organic carbon in bedrock of the Whataroa catchment is well organized as it was exposed to peak metamorphic temperatures of at least 300°C. We therefore expect that the chemical weathering is likely to be a small component (smaller than 10–15%) of the fossil organic carbon flux, with negligible oxidation occurring during the riverine transit [*Hilton et al.*, 2011]. Based on the above observations, we assume that there is no fractionation and that structure of the fossil organic carbon in bed load is not distinct from the fossil organic carbon in suspended load.

3. The Provenance of Detrital Sand

In this section, we describe our sampling strategy, report the concentration of TOC in the bedrock, and report our RSCM-*T* measurements on detrital sand samples.

3.1. Sampling Strategy

Samples of sand were collected from gravel bars within river and stream channels in the Whataroa catchment to investigate how the distribution of detrital RSCM-*T* evolves downstream (Figure 4). Sites were selected

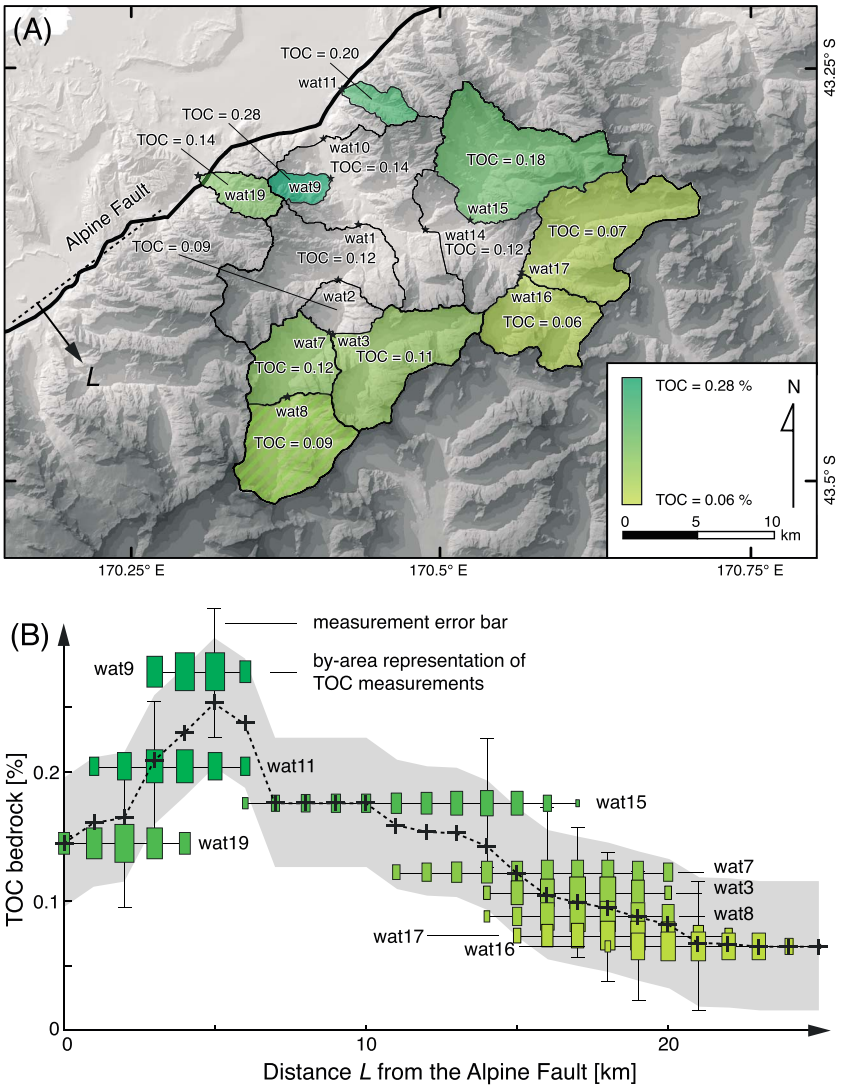

Figure 4. (a) TOC content measured in several detrital sand samples of the Whataroa and adjacent catchments. Small catchments, which were used in the following TOC variation estimation (Figure 4b) are marked with green color according to TOC content. Sampling sites are labeled and TOC content (%) is indicated in the catchment polygon (measurement accuracy = ± 0.05%). (b) Approximate estimate of TOC variations in bedrock in direction *L* perpendicular to the trace of the Alpine Fault (as indicated in Figure 4a). The size of the green measurement rectangles represents catchment area parallel to the trace of the Alpine Fault. The final estimation (dashed line) and its uncertainty (grey shades area) was calculated using this by-area representation.

so that the samples represented collections of material eroded from subcatchments of different scale and across different bedrock lithology. At major river junctions two samples were taken, one from each upstream channel, at least 200 m away from the next upstream tributary channel. Samples were immediately dried in the field and then packed and sealed in plastic bags.

3.2. Variations of Tracer Abundance in Bedrock

We used a coulometric method to measure TOC content in sand samples from small tributaries draining areas of approximately uniform bedrock, rather than the bedrock directly, because large variations in TOC can occur at outcrop scale. For the reasons mentioned in the previous section, we assume that the TOC measurements presented in Figure 4a and Table 1 represent fossil organic carbon from bedrock. The coulometer measures total carbon (TC) and total inorganic carbon (TIC) content by measuring CO_2 released from a sample by combustion (TC) or acidification (TIC). Finally, TOC is calculated by subtracting the TIC from the TC result. More information about coulometric TOC estimation in general can be found in *Engleman et al.* [1985].

Table 1. Results of the TOC Analysis of Detrital Sands From Several Whataroa Subcatchments, From Abrasion Experiment EN2 Conducted With Schist Pebbles and EN4 Conducted With Sandstone Pebbles (See Appendix A and Table 2 for Further Explanation)[a]

Sample Name	Total Carbon (%)	Total Inorganic Carbon (%)	Total Organic Carbon (%)
wat1	0.17	0.05	0.11
wat1 (second)	0.19	0.05	0.14
wat2	0.14	0.05	0.09
wat3	0.12	0.01	0.11
wat7	0.22	0.10	0.12
wat8	0.13	0.05	0.09
wat9	0.29	0.01	0.28
wat10	0.16	0.02	0.14
wat10 (second)	0.16	0.01	0.14
wat11	0.25	0.05	0.20
wat14	0.16	0.03	0.12
wat15	0.23	0.05	0.18
wat16	0.08	0.01	0.06
wat17	0.08	0.01	0.07
wat19	0.18	0.03	0.14
EN2	0.48	0.06	0.42
EN2 (second)	0.38	0.06	0.32
EN4	0.33	0.13	0.20

[a]wat1, wat10 and EN2 have been measured twice, indicating accurate TOC measurements.

For TIC analysis, samples were weighed into small glass capsules that were placed into a test tube. The test tube was attached to the acidification module (CM5130 Acidification Module) and 2.5 mL of 2N perchloric acid was added to dissolve the carbonate minerals and set free the CO_2 gas that was introduced into the coulometer cell. A heating device that accelerates dissolution of the minerals was used. For TC measurement, the samples were weighed into tin capsules and burned in a combustion tube at 950°C (CM5200 Autosampler/Furnace). In this study, we analyzed 40–90 mg of dry, homogenized, and finely ground rock powder samples. Additionally, two sand samples from single abrasion experiments were analyzed. Results are given in %C. For approval, standard samples (99.95% $CaCO_3$: 12%C) were measured at the beginning and at the end of each run. Estimated measurement error, taking into account weighing uncertainties is < 0.05%C.

TOC variations in the Southern Alps are revealed across the orogen. TOC content, measured in small- to medium-area subcatchments show a systematic shift from values less than 0.1% near the main divide crest in the southeast, increasing to 0.2% about 12 to 5 km away from the Alpine Fault and decreasing back down to 0.14 and 0.2% in its near vicinity. Plotting TOC concentration in small tributaries against distance from the Alpine Fault highlights that the TOC content varies by a factor of 2 to 3 (Figure 4b). Consequently, if erosion were uniform the detrital samples in the lower end of the Whataroa catchment should have a higher probability of containing carbonaceous particles derived from schist than sandstone.

3.3. RSCM-*T* Data Acquisition and Results in Detrital Sands

Raman spectroscopy can be used on raw material with no prior chemical and/or physical extraction of carbonaceous material. Here the sand size fraction was extracted from each sample by sieving, then gently ground to a fine powder and flattened as a thin layer on a glass plate for Raman Spectroscopy analysis. Raman spectra were obtained using a Renishaw InVIA Reflex microspectrometer. We used a 514 nm Modulaser argon laser in circular polarization. The laser was focused on the sample by a DMLM Leica microscope with a 50X objective (NA = 0.75), and the laser power at the sample surface was set to less than 1 mW. The Rayleigh diffusion was eliminated by edge filters, and the signal was finally dispersed using a 1800 gr/mm grating and analyzed by a Peltier cooled RENCAM CCD detector. Before each session, the spectrometer was calibrated with a silicon standard. Because Raman spectroscopy of Carbonaceous Material can be affected by several

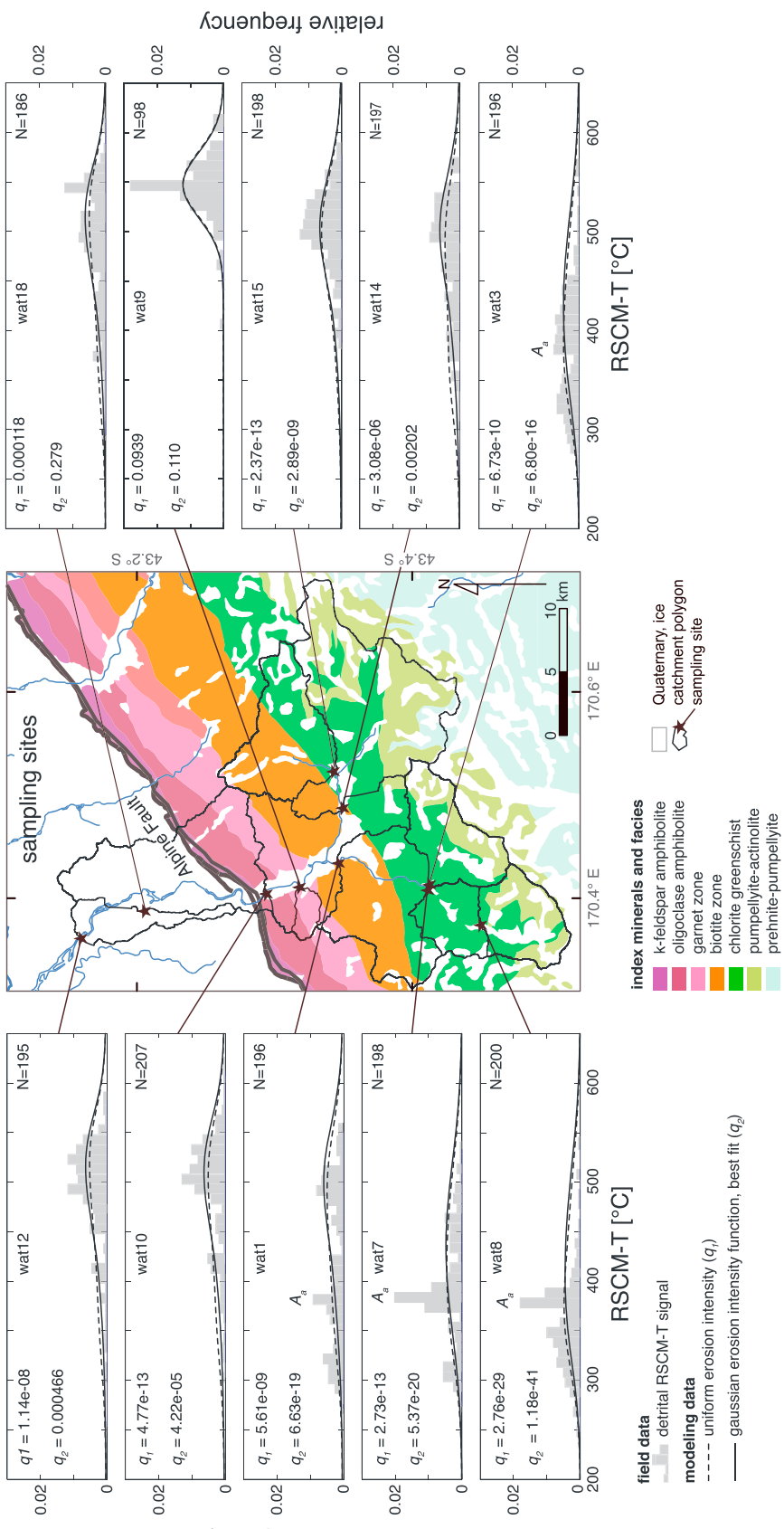

Figure 5. Temperature analyses (grey) and model predictions (solid and dotted black lines) are shown for 10 sampling sites in the Whataroa catchment. Sample name for each locality is indicated in the top center, the number of obtained spectra *N* in the top right corner of each histogram. The histograms are connected to a central geological map, showing sampling site and the associated subcatchment polygon. Note that wat9 represents a small side catchment draining high-grade schist only. All model predictions are corrected for tracer abundance, granulometry of sediment input, and bed load modifications. The black solid line represents model prediction assuming uniform erosion intensity, and the dashed black temperature signal represents best fit erosion intensity (including bed load modifications, as discussed in the text and seen in Figure 11, solid line). The values q_1 (uniform erosion) and q_2 (best fit) are displayed for each sampling site. A prominent temperature anomaly A_a is highlighted in the histograms where present.

analytical mismatches, we followed closely the analytical procedure described by *Beyssac et al.* [2002] and *Beyssac and Lazzeri* [2012].

Between 110 and 230 particles of carbonaceous material per sample were analyzed. Where a large variability of spectra was observed during the first 100 measurements, more data points were collected. Each measurement included 3 to 12 accumulations of 5 to 300 s acquisition time, depending on the signal-to-noise ratio. Due to increasing peak width, spectra of moderately organized carbonaceous material were analyzed in extended mode for a larger spectral window to correctly define the baseline (e.g., 500 to 2000 cm^{-1}). The observed Raman spectra were then automatically fitted using the method described in *Sparkes et al.* [2013]. Two different temperature correlations are applied in this software: the calibration from *Beyssac et al.* [2002] at higher temperatures from 330 to 650°C and the correlation established by *Lahfid et al.* [2010] at lower temperatures between 200 and 330°C. In the present study, all spectra (either in bedrock or in detrital sediments) were fitted using this software which automatically shifts from one calibration to the other. Note that for the bedrock samples, we use raw data for all spectra in each sample including those analyzed on detrital graphite. This yields difference with the data set presented in O. Beyssac et al. (submitted manuscript, 2015) and in Figure 2 where bedrock metamorphic temperatures are calculated on the average of all spectra with the exclusion of the ones obtained on detrital graphite. In addition, O. Beyssac et al. (submitted manuscript, 2015) use a manual fitting procedure, which involves minor RSCM-*T* differences with respect to our automatically fitted data. However, to maintain a certain consistency in our provenance analysis study, it is more appropriate to apply the same automated fitting procedure for both bedrock and detrital samples.

Detrital carbonaceous material was analyzed in 10 sand samples. Results are presented in Figure 5 in the form of normalized frequency distributions. They reveal a systematic evolution of the detrital RSCM-*T* signal, ranging from 250 to 400°C close to the main divide, and increasing to 500–640°C toward the Alpine Fault. This is in good agreement with metamorphic zones and RSCM-*T* patterns in bedrock (see Figures 2 and 3).

The width of the distribution partly reflects the subcatchment area, being significantly higher in large subcatchments that include several metamorphic zones. Small subcatchments consisting of a single bedrock lithology (or metamorphic zone) exhibit a near-normal distribution of RSCM-*T*. However, some high-*T* spectra were observed in sand samples collected in the upper domain of the Whataroa catchment (e.g., wat3 and wat7) where bedrock has only been affected by low-grade metamorphism. A similar phenomenon was observed for in situ bedrock samples, which is interpreted to reflect the presence of some remnant detrital graphite within the sandstone bedrock (see also O. Beyssac et al., submitted manuscript, 2015). Highly ordered carbonaceous material, including graphite, is very resistant to weathering and can be preserved during a whole erosion cycle [*Galy et al.*, 2008]. A noteworthy temperature anomaly (A_a, Figure 5) expressed by a distinct peak at 375°C, followed by a less pronounced depression at 360°C, is observed in several samples in the upper reaches of the Whataroa and is discussed below.

4. Abrasion Experiments

Bed load grain size reduction during fluvial transport occurs in response to abrasion, which for the purpose of this study is defined as a process that comprises fragmentation and attrition that produce particles larger and smaller than 0.5 mm, respectively. It depends on the lithology, initial grain size distribution of sediment input, shape of clasts, as well as the relative and absolute abrasion rates as a function of pebble lithology and texture (e.g., *Attal and Lavé* [2009] for a discussion]. It is commonly described by Sternberg's law [*Sternberg*, 1875]:

$$D = D_0 e^{-\frac{k}{3} L_t} \tag{1}$$

where D_0 = initial grain size (mm), D = grain size (mm), L_t = travel distance (km), and k = grain size constant (km^{-1}). Most studies have focused on quantifying pebble abrasion processes (i.e., constraining k) using tumbling mills or circular flumes over a century [*Gregory*, 1915; *Wentworth*, 1919; *Marshall*, 1927, 1929; *Krumbein*, 1941, 1942; *Kuenen*, 1956; *Bradley*, 1970; *Bradley et al.*, 1972; *Brewer*, 1991; *Brewer and Lewin*, 1993; *Cox and Nibourel*, 2015]. Here we use a similar approach and, in addition, concentrate on the size and distribution of particles produced by pebble abrasion. Depending on the type of degradation process, texturally very different lithologies are expected to generate different grain size distribution and quantity of abrasion products.

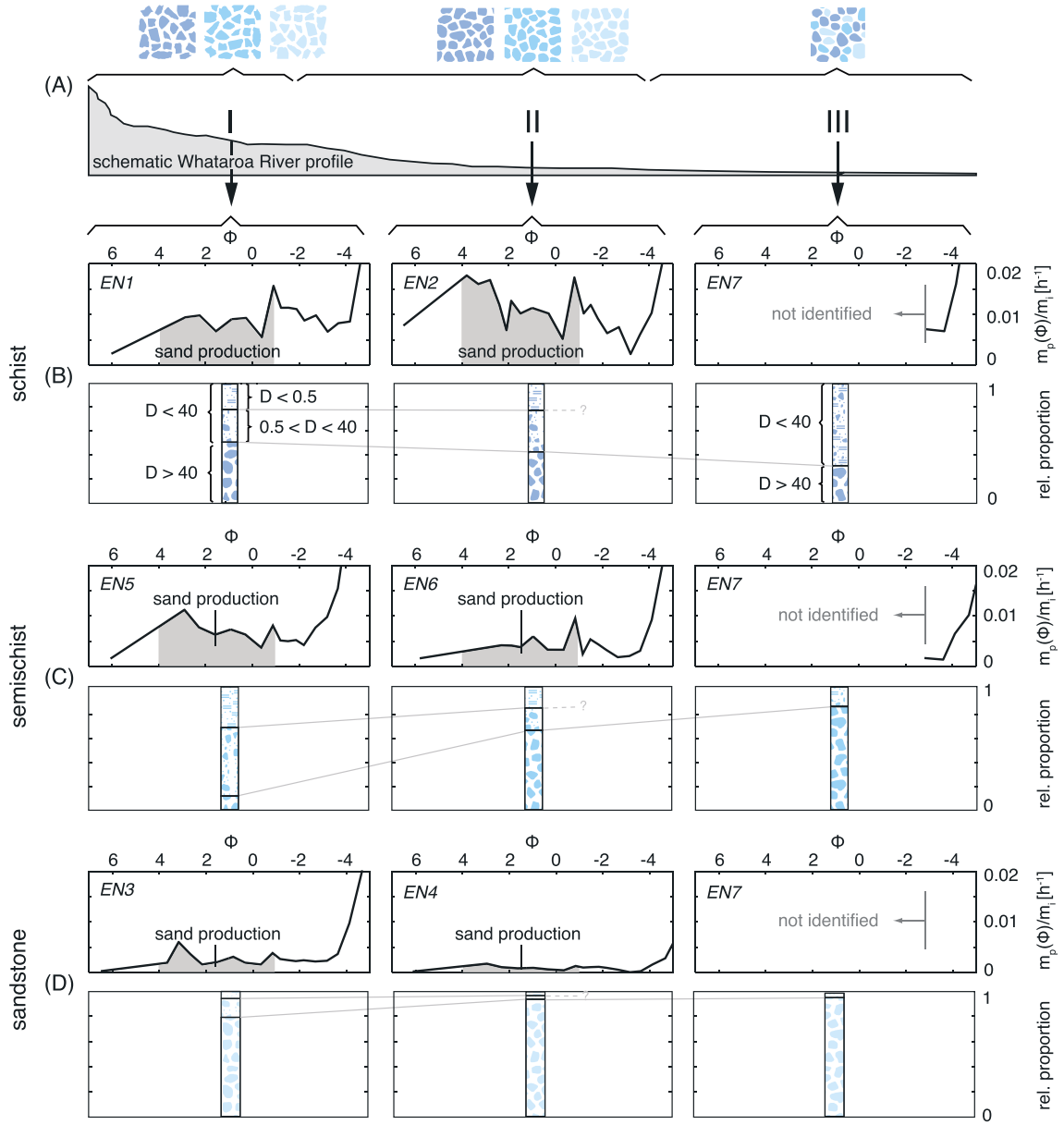

Figure 6. Abrasion experiments. (a) Schematic sketch of the Whataroa River profile. The experiment pebble input was chosen according to the three discrete zones I, II, and III where the bed load characteristics change along the river's path. The results (b) for schist, (c) for semischist, and (d) for sandstone. The top plots of each lithology show grain size distributions of abrasion products ($m_p(\phi)$, black line) normalized to input mass m_i. All granulometric distributions of abrasion products were normalized to unit time = 1 h. The area covering the sand size fraction is shaded grey. The lower plots of each lithology illustrate the evolution of abrasion, attrition, and fragment production rates as a function of bed load characteristics (I to III). The *D* indicates bounds of each grain size class (in millimeters). All rates are normalized to unit time = 1 h and unit input mass = 1.

4.1. Experimental Device

To document abrasion processes, we used a large annular flume device developed and tested by *Attal and Lavé* [2006], *Attal et al.* [2006], and *Attal and Lavé* [2009]. Unlike most pebble abrasion experiments, this device reproduces impact velocities and hydrodynamic conditions that are equivalent to a natural river at flood [*Attal and Lavé*, 2006]. This enables us to derive absolute values of abrasion rates in mass loss per time and unit distance that are used in Sternberg's law. In order to simulate bed load abrasion in the different environments of a catchment, we first use angular material of a given lithology then mix this together with rounded river pebbles of the variety of lithologies present in the Whataroa catchment, instead of using rounded pebbles only. See Appendix A for further information.

Table 2. Summary of Input of Abrasion Experiments and Abrasion and Particle Production Rates, Obtained in 7 Abrasion Experiments[a]

		Input Mass	Run Time	Abrasion		Attrition		Fragmentation		Sand Production	
	Experiment Type	m_i	t	$^{abr}E_t$	$^{abr}E_d$	$^{att}E_t$	$^{att}E_d$	$^{frag}E_t$	$^{frag}E_d$	$^{sand}E_t$	$^{sand}E_d$
Lithology	(Name)	(kg)	(min)	(%h^{-1})	(%km^{-1})	(%h^{-1})	(%km^{-1})	(%h^{-1})	(%km^{-1})	(%h^{-1})	(%km^{-1})
	I (EN1)	44.49	25	49.0%	9.1%	21.5%	4.0%	27.5%	5.1%	9.7%	1.8%
Schist	II (EN2)	39.29	50	**57.0**%	**10.6**%	22.1%	4.1%	34.9%	6.5%	9.8%	1.8%
	III (EN7)	14.29	50	67.3%	12.5%	-	-	-	-	-	-
	I (EN5)	43.86	25	88.9%	16.5%	33.4%	6.2%	55.5%	10.3%	7.6%	1.4%
Semischist	II (EN6)	40.38	49	**35.7**%	**6.6**%	17.6%	3.3%	18.1%	3.4%	5.2%	1.0%
	III (EN7)	14.75	50	18.4%	3.4%	-	-	-	-	-	-
	I (EN3)	29.17	50.5	20.8%	3.8%	5.8%	1.1%	15.0%	2.8%	2.5%	0.5%
Sandstone	II (EN4)	34.52	51.7	**6.2**%	**1.2**%	3.4%	0.6%	2.9%	0.5%	1.1%	0.2%
	III (EN7)	11.27	50	3.3%	0.6%	-	-	-	-	-	-
Granite	III (EN7)	5.74	50	16.6%	3.1%	-	-	-	-	-	-
Ultramafics	III (EN7)	2.02	50	3.6%	0.7%	-	-	-	-	-	-

[a]The pebble characteristics I, II, and III refer to clast rounding, fluvial preselection of more durable clasts and mixing of lithologies as specified in Figure 6a. Abrasion rates of experiments EN2 (schist), EN6 (semischist) and EN4 (sandstone) that were used in the model (see section 5.2) are in bold.

4.2. Experimental Procedure

Experiments were organized to represent three "zones" to reflect the fluvial disaggregation processes of river sediment going from the upper alpine region down to the alluvial plain in the foreland northwest of the Alpine Fault (Figure 6a). The first zone (zone I in Figure 6a) corresponds to head-water channels in the catchment, where channels incise bedrock or young colluvial deposits. Sediment supply not only is dominated by fresh landslide [*Hovius et al.*, 1997; *Korup et al.*, 2004; *Allen et al.*, 2011], debris flow, and talus material but also includes erosion of colluvial deposits and glacial till. The second zone (zone II in Figure 6a) corresponds to an intermediate region where channels incise colluvium, fan deposits, and some bedrock gorges. As the sediment load of the river reaches this intermediate stage, most pebbles are moderately rounded. Although there is some supply of new angular sediment, rounded pebbles are a preselection of more durable rock fragments, as many weak clasts have not survived. Finally, The third and last zone (zone III in Figure 6a) corresponds to the downstream alluvial channel in the vicinity of the Alpine Fault and further to the northwest. Here the main river channel is armored with boulders, and sediment supply is dominated by erosion of riverbanks composed of older alluvium or alluvial fan deposits. In the lower reaches, the degree of rounding and preselection of stronger pebbles is elevated and bed load also includes additional lithologies derived from the northwestern side of the Alpine Fault. See Appendix A for further information.

Seven experiments were run; two for each lithology (for schist: experiments EN1 and EN2, for semischist: experiments EN5 and EN6, and for sandstone: experiments *EN*3 and *EN*4) separately, and one with mixed lithologies altogether (experiment EN7) (see Table 2).

4.3. Quantification of Mass Loss and Mass Production

Attal et al. [2006] and *Attal and Lavé* [2009] introduced different specific rates of mass loss and particle production during pebble abrasion. For better comparability, all rates are expressed in mass loss, relative to total input mass per unit time E_t and traveled distance E_d ($E_d = E_t/U_p$), respectively, where U_p is the mean pebble velocity. They are calculated as follows:

$$E_d = \ln(m_i/m_p)/L_t \tag{2}$$

where m_i is the initial weight of a given rock category and m_p is the weight of material of a given grain size (D) class. The following abrasion and particle production rates are used in this study: (1) abrasion rate $^{abr}E_t$ (h^{-1}) and $^{abr}E_d$ (km^{-1}), which quantifies the total mass loss of clasts larger than $D = 40$ mm and is equal to the sum of attrition rate and fragment production rate; (2) attrition rate $^{att}E_t$ (h^{-1}) and $^{att}E_d$ (km^{-1}), which corresponds to the production rate of particles smaller than $D = 0.5$ mm; (3) fragment production rate $^{frag}E_t$ (h^{-1}) and $^{frag}E_d$ (km^{-1}) which corresponds to the production rate of particles between $D = 0.5$ mm and $D = 40$ mm; and (4) we introduce a sand production rate $^{sand}E_t$ (h^{-1}) and $^{sand}E_d$ (km^{-1}) which corresponds to the rate of sand particle production ($0.063 < D < 2$ mm) during tumbling. (Note that $^{att}E_d = k(U_p)^2$.)

4.4. Characterization of Pebble Abrasion

The systematic analysis of abrasion products enables us to describe granulometric distributions of abrasion products, normalized to input mass per time or per traveled distance. The grain diameter D is generally plotted on a logarithmic scale [*Wentworth*, 1919] where:

$$D = 2 \times \exp -\phi \tag{3}$$

4.5. Experimental Results

For all seven experiments, we discuss the following: (1) the evolution of the granulometric distribution and (2) the evolution of abrasion, attrition, fragmentation, and sand production rates for our three rock categories. Reported values are provided in Table 2 and plotted in Figure 6 (blue bars).

Three major observations can be made through comparison of the granulometric distribution and abrasion rates of schist, semischist, and sandstone. First, the abrasion rates of semischist and sandstone are lower in experiments with increased degree of pebble preselection and rounding (experiments EN5 cf. EN6 and EN3 cf. EN4, respectively). Fragmentation rates were particularly elevated during the initial abrasion of angular clasts of semischist and sandstone (experiments EN5 and EN3). Second, by way of contrast, schist abrasion rates were lowest in the experiment with angular clasts (EN1) and increased with progressing pebble rounding and preselection (EN2). Schist pebbles reduced their size most efficiently when mixed with more durable lithologies such as sandstone and semischist (EN7). Third, the rates of sand production of the main lithologies correlate with the total abrasion rates.

4.5.1. Schist

The experimental results for schist clasts are shown in Figure 6b. Production of particles larger than 4 mm (-1ϕ) dominated experiment EN1 with angular clasts representing zone I. In experiment *EN*2 with rounded and preselected pebbles, production of particles smaller than 0.5 mm (1ϕ) was dominant. Very high rates of abrasion appear to result from both processes; surface attrition and fragmentation. Interestingly, we observe higher abrasion rates during the second experiment compared to EN1, which contrasts with other abrasion studies [*Kuenen*, 1956; *Brewer and Lewin*, 1993]. Perhaps more importantly, the highest schist abrasion rates were observed in experiment EN7 representing zone III, in which rounded and preselected schist pebbles were tumbled with other more durable lithologies.

4.5.2. Semischist

The granulometric distribution of abrasion products as well as the evolution of abrasion, and particle production rates of semischist are shown in Figure 6c. We observed the highest fragment production rates during experiment EN5. Surprisingly, angular clasts of semischist had higher abrasion rates than angular clasts of schist in experiments representing zone I (the first few kilometers of transport). Abrasion rates are lower in EN6, and by an order of magnitude in EN7 when compared with EN5, indicating that the abrasion of semischist decreases significantly between zones I and III. Accordingly, sand production rate ($^{sand}E_t$ (h^{-1})) decreased from 7.6% h^{-1} in experiment EN5 (zone I) to 5.2% h^{-1} for EN6 (zone II).

4.5.3. Sandstone

Experimental results for the abrasion of sandstone clasts are presented in Figure 6d. Comparison of the abrasion rates between experiments EN3, EN4, and EN7 suggests that sandstone clasts exhibit typical asymptotically decreasing abrasion rates, similar to those observed for semischist clasts, but with rates being up to 1 order of magnitude lower. Sand particle production was generally low and descended from $^{sands}E_t$ (h^{-1}) = 2.5%h^{-1} in EN3 down to 1.1% h^{-1} in EN4. Fragmentation appears to be the dominant process of angular sandstone abrasion in experiment EN3 representing zone I, but for preselected and rounded pebbles in experiment EN4 representing zone II, surface attrition to produce fine particles was equally important.

4.5.4. Mixed Lithologies

In experiment EN7 rounded pebbles of different lithologies were abraded together in order to study the disaggregation of polymictic bed load having different rock strength properties as expected in zone III. The experiments results are presented in Figure 7. The source of sand size and very fine gravel ($\phi > -2.2$) products could not be readily identified by eye, so was estimated using a proxy from the RSCM-*T* distribution of carbonaceous material in the sand.

In experiment EN7 schist pebbles abraded faster than semischist and sandstone, decreasing in relative abundance in larger gravels $D > 40$ mm, but producing relatively large amounts of finer-grained products.

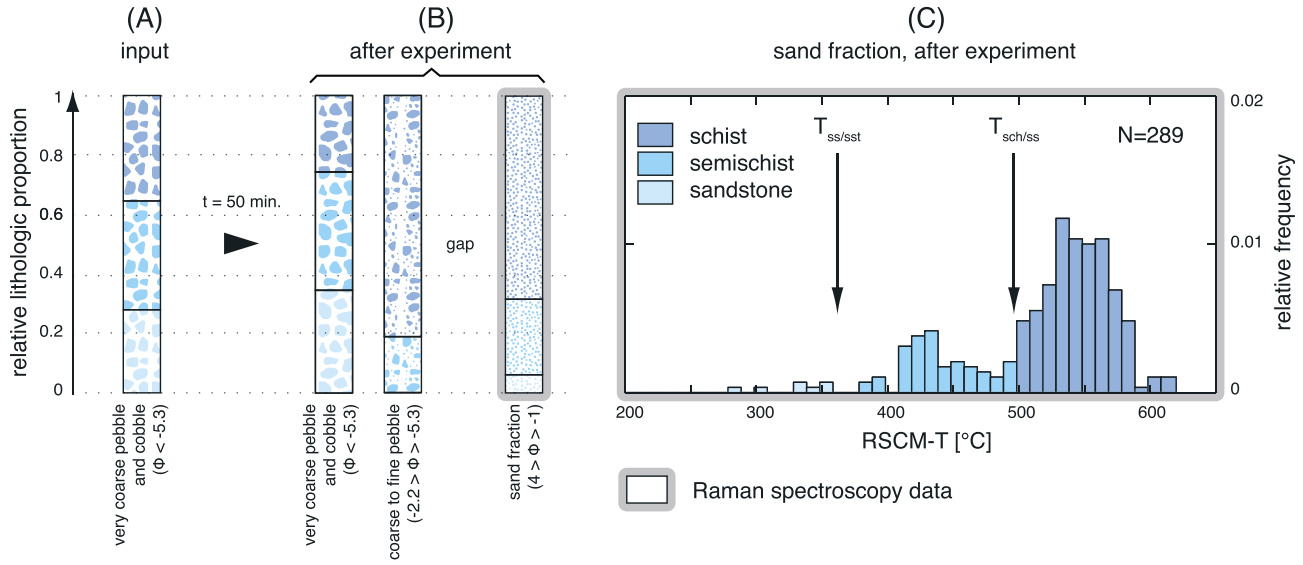

Figure 7. Results from the mixed lithology experiment (EN7) showing (a) relative lithologic proportion of sediment input compared to (b) lithologic proportion of abrasion products after tumbling in three grain size classes. Lithologic proportion of sand size particles was estimated using RSCM. (c) RSCM-data collected for sand derived from the experiment including the applied temperature bounds $T_{ss/sst}$ and $T_{sch/ss}$. Note that relative lithologic proportion for grain sizes greater than 5 mm refers to percent per mass, whereas the lithologic proportions of sand size particles (measured using RSCM) reflects a volume percent.

From an initial input of 26%, the relative abundance of schist in gravel and sand abrasion products reached between 81% and 68% of total mass for $D < 40$ mm (Figures 7a and 7b). In contrast, the relative abundance of sandstone pebbles increased within the larger grain size class.

The relative abundance of abrasion products changed as a nonlinear function of grain size class, with changes being most pronounced for small gravels ($5 < D < 40$ mm). In the sand size window, of particular interest in this study, relative lithologic abundance appears to have been strongly distorted compared with input ratios. RSCM-*T*-based estimates suggest from an initial input of 22% of the sediment, sandstone only produced 6% of sand size particles, whereas from an input of 28% the schist produced 64% of the sand particles.

5. Modeling a Synthetic Detrital RSCM-*T* Signal

5.1. Model Description

We now use an integrative model to simulate the RSCM-*T* (*T*) field data. The model, described in detail in *Attal and Lavé* [2006], accounts for bed load modifications during transport as well as tracer bedrock concentration, spatial variations in erosion and the initial grain size distribution of sediment delivered to the fluvial network. Since the grain size fraction of interest in this study is the sand, and not the pebble fraction, the model of *Attal and Lavé* [2006] was slightly modified to track the sand composition instead of the pebble lithologic composition.

The model assumes that in a given river section, the sediment load size-distribution results from the contribution from all the parts of the watershed, modulated by the local erosion rate (or hillslope sediment supply rate) and by transport related disaggregation processes. The sand and silt fraction of the sediment in any point of the fluvial network represents the sum of the fine load initially provided by hillslope processes plus the attrition products resulting from the abrasion of coarser bed load. If we assume first that the sand/silt load is transported along rivers without major size reduction, mostly because of viscous damping [*Schmeeckle et al.*, 2001; *Scheingross et al.*, 2014], second, that most of the material supplied by the hillslopes can be transported along the fluvial network whatever its initial size is (except for very large blocks that represent a minor contribution to total sediment flux), third that abrasion does not depend on grain size, i.e., that abrasion can be encapsulated by Sternberg's law, and finally, that the system is at steady state (so that gravel and sand fraction can be associated to the same hillslope flux, even if they do not travel at the same velocity along

the fluvial network), then the detrital T spectrum can be written as an integral term on the entire upstream fluvial network (fn):

$$f(T) = \frac{\int\int_{\mathrm{fn}} A(\vec{x})\dot{\epsilon}(\vec{x})TOC(\vec{x})f(m(\vec{x}),T)\left[p^{S}_{0,j(\vec{x})} + p^{G}_{0,j(\vec{x})}(1-e^{{}^{\mathrm{abr}}E_{d,j}L_t(\vec{x})})\right]\mathrm{d}\vec{x}}{\int\int_{\mathrm{fn}} A(\vec{x})\dot{\epsilon}(\vec{x})\mathrm{TOC}(\vec{x})\left[p^{S}_{0,j(\vec{x})} + p^{G}_{0,j(\vec{x})}(1-e^{{}^{\mathrm{abr}}E_{d,j}L_t(\vec{x})})\right]\mathrm{d}\vec{x}}, \quad (4)$$

where $A(\vec{x})$ represents the local sediment contributing area, $\dot{\epsilon}(\vec{x})$ the corresponding local erosion rate, $TOC(\vec{x})$ the local tracer bedrock concentration, and $p^{S}_{0,j(\vec{x})}$ and $p^{G}_{0,j(\vec{x})}$ the local proportion of the lithology j in the sand/silt fraction ($D<2$ mm) and the gravel fraction ($D\geq 2$ mm) respectively, ${}^{\mathrm{abr}}E_{d,j}$ the abrasion coefficient that characterizes the lithology j, $L_t(\vec{x})$ the transport distance along the fluvial network between the sediment source in $\vec{x}$ and the considered sampling site, and $f(m(\vec{x}),T)$ the T distribution in the metamorphic unit m with $\int_T f(m(\vec{x}),T)\mathrm{d}T = 1$. The integrative equation (4) is solved numerically along the synthetic fluvial network extracted from the Shuttle Radar Topography Mission 90 m digital elevation model and defined above a threshold area of 1 km^2. During the first kilometers of transport, clast abrasion generally operates at a faster rate than farther downstream, because of edge-rounding processes of angular pebbles [*Krumbein*, 1941; *Kuenen*, 1956; *Pearce*, 1971]. This increased size reduction is accounted for in the model by an exponential decrease of the abrasion coefficient from $3 \times {}^{\mathrm{abr}}E_{d,j}$ to ${}^{\mathrm{abr}}E_{d,j}$ in ~ 5 km. A standard one-dimensional Kolomgorov-Smirnov test [*Massey*, 1951] was performed to evaluate the goodness of fit at each sampling site. The value q_a represents the average q value of all 10 sampling sites in the Whataroa catchment.

5.2. Model Input

In an attempt to invert this integrative model for retrieving the spatial erosion distribution, we thus need five independent data sets:

First, the distribution of T in a detrital sand depends on the T pattern in bedrock within its subcatchment area (see Figure 5). In this model, this pattern is characterized by normal PDFs (P_m) of T for each mth metamorphic unit:

$$P_m(T,\sigma_m,\mu_m) = \frac{\exp\frac{-(T-\mu_m)^2}{(2\sigma_m^2)}}{\sqrt{2\pi}\sigma_m} \quad (5)$$

where T is the peak temperature, μ_m is the mean, and σ_m is the standard deviation. These PDFs are shown in Figures 3 and 8d.

Second, the contribution from each metamorphic unit must be weighted by the land area it represents within the catchment. Figure 8a shows histograms of the relative area of each metamorphic unit as a function of the distance L to the Alpine Fault and mean T, calculated for sampling site wat18.

Third, the sand contribution by pebble abrasion during fluvial transport varies between different lithologies and, therefore, needs to be defined. We use abrasion product granulometry for textural, as opposed to metamorphic, units as they better reflect physical rock properties. Figure 8b depicts the relative land area of schist, semischist, and sandstone (Figure 1), as a function of the distance L to the Alpine Fault and mean T. We use abrasion coefficients derived from flume experiments EN2, EN6, and EN4: ${}^{\mathrm{abr}}E_{d,\mathrm{schist}}=10.6\%\ \mathrm{km}^{-1}$, ${}^{\mathrm{abr}}E_{d,\mathrm{semischist}} = 6.6\%\ \mathrm{km}^{-1}$ and ${}^{\mathrm{abr}}E_{d,\mathrm{sandstone}} = 1.2\%\ \mathrm{km}^{-1}$. For each lithology, we also use the experimentally derived distribution of abrasion products to define the proportion falling within $\phi = [-1;4]$, which corresponds to the sand size analyzed for T. The granulometry of abrasion products is shown in Figure 8c.

Fourth, the initial grain size distribution of sediment supplied to the river may also affect a downstream detrital sand sample. It defines the initial amount of sand as well as the volume and size of particles to be abraded during fluvial transport. Bedrock landslides have been shown to be the dominant process of physical denudation in this mountain belt [*Hovius et al.*, 1997; *Korup et al.*, 2004] and, therefore, are the dominant process of sediment supply. However, to our knowledge, no field data exists for granulometric distributions in Whataroa catchment or from the central Southern Alps, although some clast distributions are published from alluvial outwash plains and rock avalanche deposits [e.g., *McSaveney*, 2002]. We rely on our field observations of the gravel-dominated (pebble-boulder) material stored in sedimentary deposits of the catchment, compared with nearby pebble-boulder material locally lining stream and river channels, or forming talus and colluvium slopes. We selected a granulometric distribution based on a field distribution measured in the Himalaya

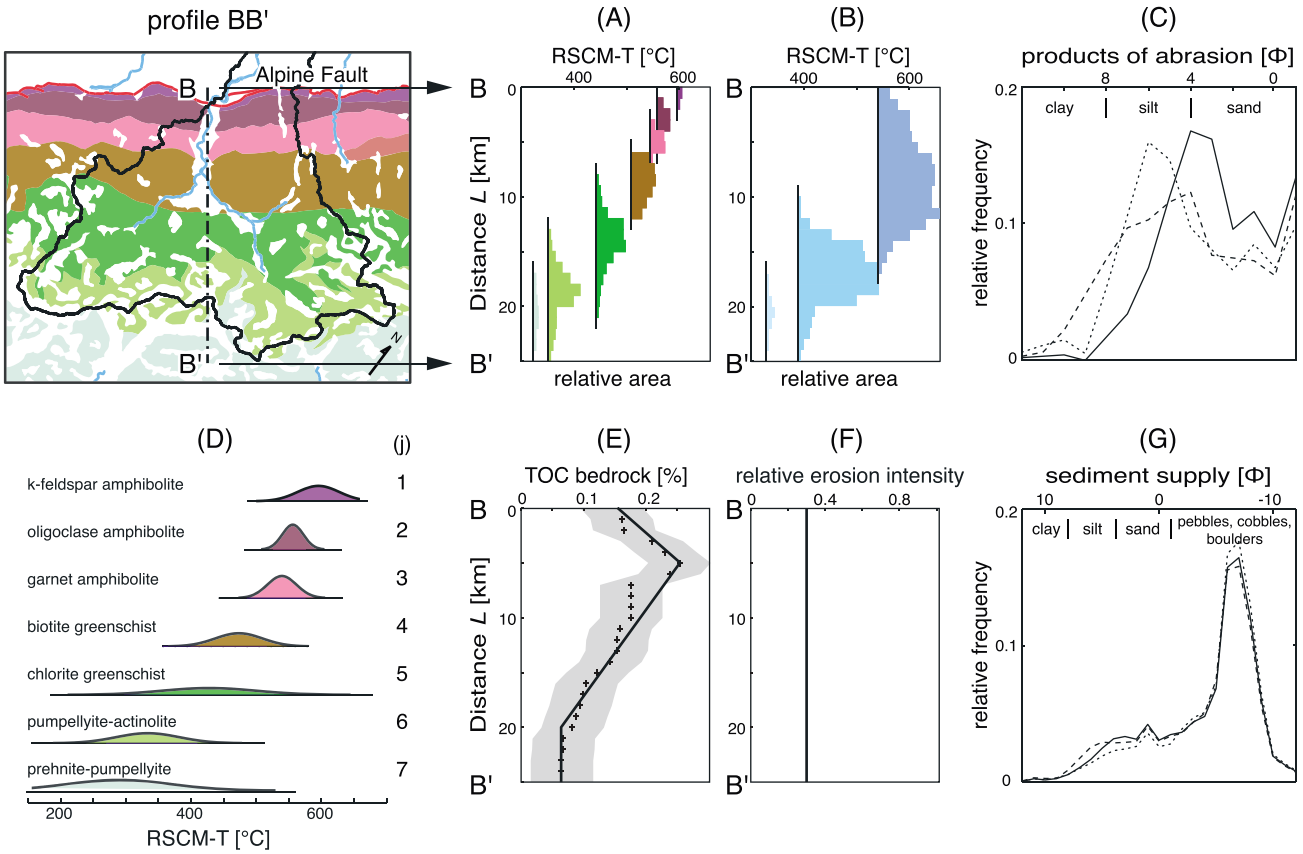

Figure 8. Input parameters: (top left) Catchment polygon wat18 on a map of metamorphic zonation. Profile BB′ is situated on a line perpendicular to the trace of the Alpine Fault. (a) Histograms representing relative area of each metamorphic zone within the catchment area of wat18 in direction of profile BB′, plotted against mean RSCM-*T*. (b) Histograms representing relative area of schist (dark blue), semischist (blue), and sandstone (pale blue) terranes within the catchment area of wat18, plotted against mean RSCM-*T*. (c) Normalized overall granulometry of abrasion products with schist (solid line), semischist (dashed line), and sandstone (dotted line). (d) Normal Gaussian distributions of RSCM-*T* as a function of metamorphic zonation, calculated from RSCM-*T* field data. (e) Tracer abundance estimate in direction of profile BB′. The black solid line represents the linear approximation of the TOC estimate (black points) and uncertainty estimate (grey shaded area). (f) Constant relative erosion intensity in direction of profile BB′. (g) Normalized granulometry of sediment supplied to the river from schist (solid line), semischist (dashed line), and sandstone (dotted line) terrains, which is from the Himalaya [*Attal and Lavé*, 2006].

[*Attal and Lavé*, 2006] that matches our field observations. The granulometric model input of schist, semischist, and sandstone by mass is shown in Figure 8g. As it is possible to have other granulometric distributions, or in the event the Himalayan model proves not to be representative of the New Zealand situation, the sediment input supply is tested in the sensitivity analysis reported below.

Fifth, the bedrock tracer concentration has a direct influence on the detrital *T* distribution. We assume that the TOC content is constantly parallel to the Alpine Fault but varies with the distance *L* from the Alpine Fault (Figure 8e), as discussed above and shown in Figure 4. The function we use in the model is shown in Figure 8e.

Sixth, spatial variations of erosion have a direct impact on a downstream detrital *T* signal. Since both exhumation and precipitation vary across, rather than along, the Southern Alps [*Woods et al.*, 2006; *Herman et al.*, 2009] we adopt a simple assumption for the model that catchment-scale erosion varies only in a direction perpendicular to the Alpine Fault (along axis *L*). Note that for sensitivity analysis, we apply uniform erosion rates of 3 mm yr^{-1} (Figure 8f). The assessment of variable erosion patterns will be discussed in section 5.4.

5.3. Model Sensitivity to Abrasion Constant, Bedrock Concentration, and Initial Grain Size Distribution

In this section, we vary the model parameters and compare model predictions to the RSCM field data at site wat18 (Figure 5). In order to investigate the sensitivity of one model parameter to another, variations of the

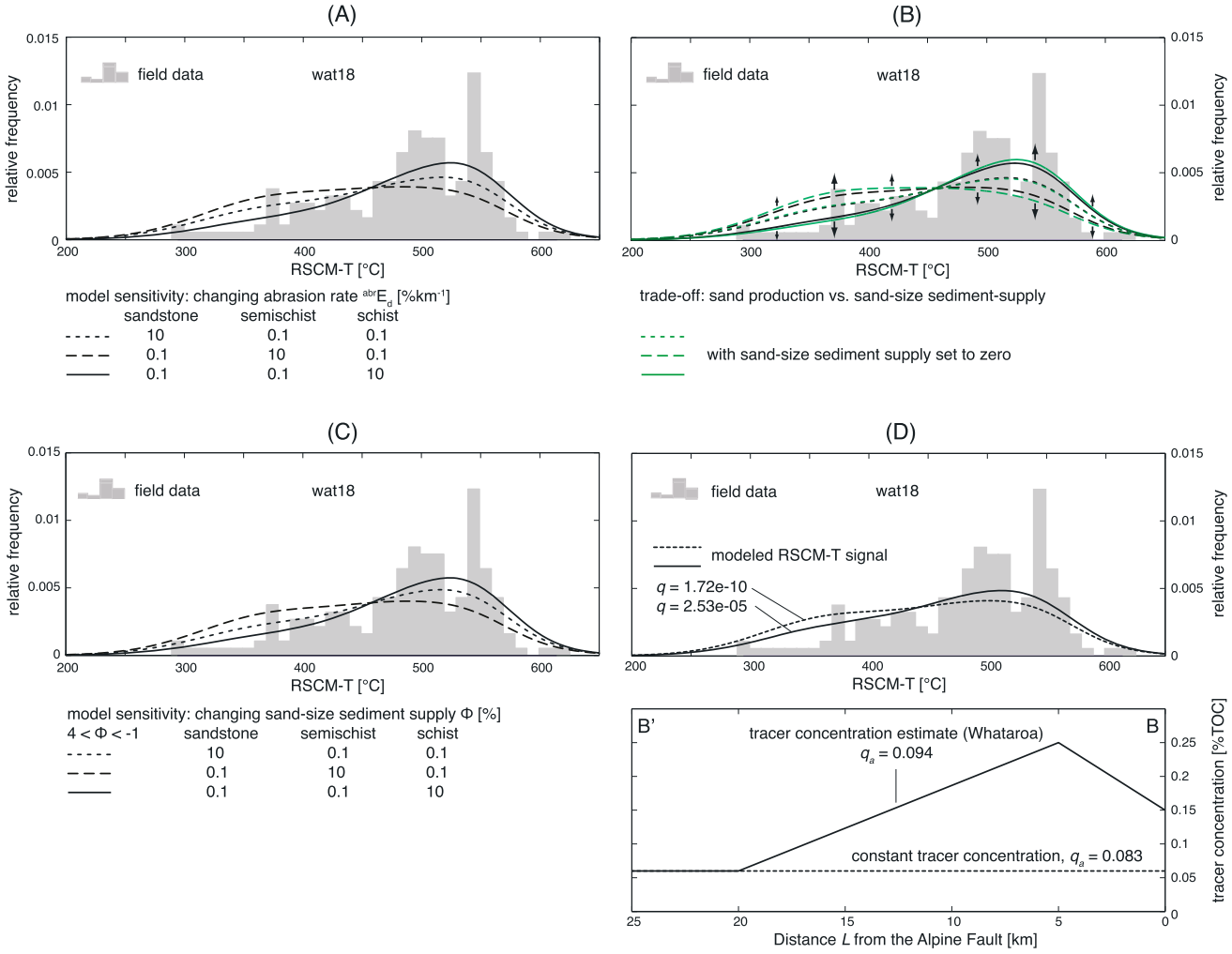

Figure 9. (a) Sensitivity analysis of bed load modifications. Modeled *T* prediction with abrasion coefficients of schist, semischist, and sandstone varying in the order of 2 magnitudes. (b) Illustration of the trade-off effect between sediment supply and abrasion rates. The green *T* signals were calculated using the same abrasion coefficients as in Figure 9a but with sand size sediment supply set to zero. (c) Sensitivity analysis of sediment supply. Three black lines represent *T* signals calculated for sand size particle content in sediment supply of the three main rock types schist, semischist, and sandstone (as indicated in the table below the plot). (d) The difference between a *T* distribution calculated for uniform tracer abundance (dashed black line) and best estimate tracer abundance (solid line). The *q* and q_a values estimating the goodness of fit in site wat18, respectively, over all sampling sites are included in the plots.

model parameter to be tested were changed by 2 orders of magnitude, while the remaining model parameters were held constant (using default input parameters as seen in Figure 8).

The effect of increasing the abrasion coefficient of one lithology with respect to the two others can be seen in Figure 9a. The lithology having the highest abrasion coefficient produces most sand at the sampling site. The effect is largest with elevated abrasion rates for semischist and schist compared to sandstone. This can be explained by the small area of exposed sandstone in the Whataroa catchment (Figure 8b). When applying abrasion rates and granulometry of abrasion products as quantified in experimental study cases, the goodness of fit over all sampling sites (q_a) decreases from 0.0115 (i.e., without bed load modifications) to 0.0094 (i.e., including bed load modifications). However, the goodness of fit for all downstream sampling sites (wat12, wat18, and wat10), where the effect of contrasting abrasion properties is considered most pronounced, increases.

The total amount of sand particles at a sampling site represents the sum of abrasion related sand production during fluvial transport plus the amount of sand initially supplied to the river by hillslope processes. The granulometry of sediment input varies as a function of rock type and is defined for three main rock types

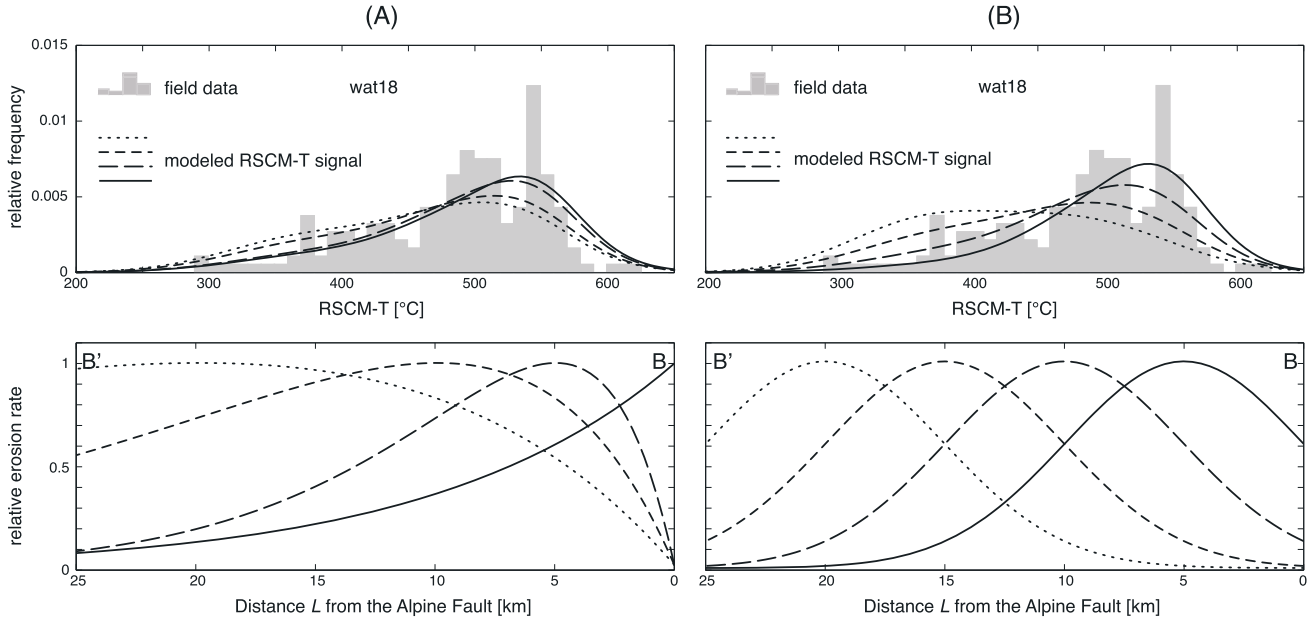

Figure 10. Sensitivity analysis of erosion intensity. (top) *T* signals, calculated for various erosion intensity functions. (bottom) The relative erosion intensity functions for the various *T* models as a function of distance *L* from the Alpine Fault. Four *T* signals calculated (a) for exponential and (b) for Gaussian erosion intensity functions.

schist, semischist, and sandstone. The effect of having one lithology supplying 100 times more sand compared to the two others can be seen in Figure 9c. The lithology supplying more sand size material dominates sand particles at the sampling site. There is a trade-off between sand produced by pebble abrasion during transport and sand delivered by sediment supply: the larger the initial input of sand size material by hillslope processes, the smaller the impact of contrasting abrasion rates, and vice versa (Figure 9b).

The model sensitivity to changes in tracer concentration can be seen in Figure 9d. Model predictions are generally more sensitive to changes in bedrock tracer concentration than other tests of sensitivity (Figures 9a and 9b). Applying the approximate estimate for TOC variations in the Whataroa (solid black line) instead of constant tracer abundance (dashed, see lower plot in Figure 9d) results in a better fit at site wat18, as well as the q_a value integrated over the entire catchment (q_a values are shown in Figure 9d, below).

5.4. Erosion Patterns From Pebble Abrasion

The pattern of erosion determines the spatial distribution of sediment supply to the river system. This is the main unknown we wish to constrain. The models presented in the previous section assume uniform erosion over the entire catchment. To keep the problem simple, we only consider long-term erosion rates ϵ to vary as function of L—the distance to the Alpine Fault. We first test exponential (Figure 10a) and then Gaussian (Figure 10b) relative erosion functions, which are described by the following equations:

$$\epsilon = (1 + c_1 L)\exp\left(-\frac{L}{c_2}\right) + c_3 \tag{6}$$

$$\epsilon = \exp\left(\frac{-((L - c_1)^2)}{{c_2}^2}\right) + c_3 \tag{7}$$

where the constants c_1, c_2, and c_3 are our tunable parameters.

For sensitivity analysis c_3 is set to zero to increase the effect of lateral erosion intensity changes. Relative erosion rates are first assumed to be highest at the Alpine Fault. We then shift the peak progressively away from it; the same procedure is adopted for the exponential (Figure 10a) and the Gaussian functions (Figure 10b). In doing so, we observe an effect of shifting the modeled *T* distributions. The model sensitivity to erosion intensity changes is comparable to the impact of the tracer concentration (Figure 10b cf. Figure 9d).

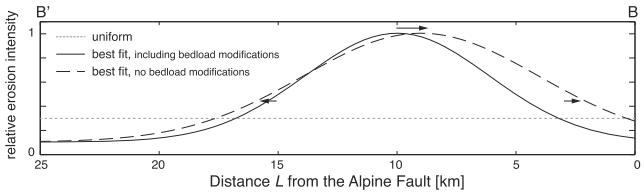

Figure 11. Best fitting relative erosion intensity function when including bed load modifications (solid line), without taking bed load modifications into account (dashed line), and for uniform erosion intensity (dashed line) plotted against distance L from the Alpine Fault (compare to profile BB' Figure 8 (top left)).

We optimize the fit to the data (i.e., maximizing q_a) by trial and error. We find that q_a increases significantly from 0.0094 for uniform erosion up to 0.0392 with a favored mode. In turn, we find the following Gaussian erosion intensity distribution:

$$\epsilon = \exp\left(\frac{-((L-10)^2)}{5.5^2}\right) + 0.1 \tag{8}$$

This implies that relative erosion rates are maximized about 10 km away from the Alpine Fault (Figure 11, black solid line). Low T signals are generally more difficult to fit. Some local features of the field data, such as the T anomaly A_a, (Figure 5) in the upper reaches of the Whataroa catchment (wat1, wat3, wat7, and wat8) are not replicated by the model predictions (see below). Note that although the model operates with absolute erosion intensity values, this best fitting spatial erosion pattern is expressed as relative and not absolute values of erosion.

The above best fitting erosion function is found using the abrasion coefficients from abrasion experiments as shown in section 5.2. In order to better illustrate the effect of bed load modifications on a downstream sand sample, we find a second best fitting erosion function, using abrasion coefficients for schist, semischist, and sandstone that are set to zero:

$$\epsilon = \exp\left(\frac{-((L-9)^2)}{7.5^2}\right) + 0.1 \tag{9}$$

When neglecting bed load modifications, the peak of the best fitting erosion function shifts approximately 1 km toward the Alpine Fault (from $L = 10$ to $L = 9$ km, see Figure 11, dashed line) and its peak width at half amplitude rises from 11 (best fit, including bed load modifications) to 15 km (best fit, no bed load modifications).

6. Discussion

Despite its apparent simplicity, the model is able to approximately replicate field data and enables us to investigate the effect of key factors controlling the T distribution in a detrital sand. Modeling of the data from Whataroa catchment suggests tracer abundance and erosion intensity have a first-order control on the detrital T signal. Although less dramatic, bed load modifications during fluvial transport and sediment input granulometry also modify the nature of detrital sands. The results must be applied with caution in that they may not apply to catchments with different geology, hydrodynamical conditions, or scale. In the following section, we discuss our interpretations of the experiment and modeling observations in detail, first with respect to each of the four key model parameters individually, then as a whole.

6.1. Evolution of the Detrital RSCM-*T* Signal

Field detrital T data variations occur at different scales. Large-scale variations can be a result of spatially variable uplift, precipitation, and mode of erosion (e.g., glacial versus fluvial erosion) having different input granulometry, bed load modifications, or tracer abundance. The model predictions we report are only appropriate at the scale of the entire Whataroa catchment. However, we observe variations at smaller scale. In particular, the spatially and temporally variable character of sediment supply to the river system is expected to produce many of these local irregularities. The effect of a single landslide event, for example, might be expected to dominate the signal measured in a small subcatchment on a short timescale. Furthermore, other effects such as local variations in tracer abundance, or weathering-related oxidation of less organized fossil organic carbon as a result of variable residence time in soils, may cause local T variations. Such local effects

determine the limits of our model in terms of spatial resolution. Nevertheless, wat9, which is a small side catchment draining garnet-amphibolite zone schist, was the best fitted of all subcatchments probably reflecting the relatively homogeneous bedrock geology.

T data from small upstream catchments were the worst fitted by the model. In wat3 and wat8, low *T* are systematically underrepresented by modeling data. This can partly be explained by the weak performance of the bedrock *T* classification in low-grade metamorphic rock. *T* measured in the chlorite zone bedrock is weakly bimodal, and pumpellyite-actinolite zone bedrock shows a similarly broad spread of values, which were approximated with a normal Gaussian distribution. The model therefore predicts wide *T* fields for upstream subcatchments draining these metamorphic zones, while the field data *T* signal of the corresponding subcatchments is more narrow. Such uncertainties could be reduced by analyzing more bedrock samples (O. Beyssac et al., submitted manuscript, 2015).

Introduction of the best fit erosion function reduces the difference between observed and modeled *T*. Local effects such as the *T* anomaly A_a (Figure 5) are not replicated by the model. This anomaly at 375° and adjacent low at 360° occurs in four subcatchments on the west (Whataroa River) side of the catchment. Its origin is unclear, but because it occurs in several subcatchments, two of them adjacent to each other, it is thought to be geological rather than a methodological bias (e.g., *T* calibration effect). Because it is observed in two spatially independent subcatchments, a single landslide event providing a large point-source quantity of sediment is excluded. Possible explanations for the anomaly include the following: (1) folding and thrusting, resulting in a regional doubling of a sequence of rock, being exhumed from the same depth and thus having similar *T*; (2) a local anomaly of TOC in bedrock, caused, for example, by thicker than normal argillite layers that were not detected in the measurement of TOC average values in detrital sands; and (3) differential relative erosion rates of rocks at a certain metamorphic grade. Such anomalies are not necessarily related to the RSCM tracer technique, but might similarly occur with any other sediment tracer technique.

Finally, this study provides no information about the mean residence time of bed load, which is mostly sporadically mobilized during floods as opposed to continuously. It is not clear if our results represent catchment erosion during the last 10, 100, or 1000 years. The effects of reworking sedimentary deposits, such as alluvial terrace deposits in the lower part of the catchment, were not addressed. The model was necessarily simplified with an assumption that at any position in the catchment, cover deposits will have experienced the same travel distance as the sediment in the nearby river channel, and just be a stored version of material in the channel. The assumption will be oversimplified where tills carried by ice are present and may be more angular than nearby alluvium in the river channel. Chemical weathering is another effect that may be important in other mountain areas. The western side of the Southern Alps possesses high chemical weathering rates but is dominated by mechanical erosion [*Jacobson et al.*, 2003; *Larsen et al.*, 2014]. Catchment-averaged rates of chemical weathering (10^3 kg km^{-2} yr^{-1}) are 2 orders of magnitude lower than rates of mechanical weathering derived from suspended sediment load (10^5 kg km^{-2} yr^{-1}). The lack of oxidation rinds on clasts in the rapidly transported bed load of the Southern Alps also suggests chemical weathering effects are locally minor and so have not been considered. Chemical weathering processes, if significant, could potentially accelerate abrasion rates or even affect the structural organization of carbonaceous material.

6.2. The Effect of Tracer Abundance Variations

Tracer abundance is a key input parameter. Variations in TOC content have a first-order impact on modeled *T* distributions where catchments or subcatchments drain more than one rock type or a wide range of metamorphic zones as shown in Figure 9d. Models tested uniform and variable TOC contents. The average q_a value, representing the Kolmogorov goodness of fit, slightly increases from q_a(uniform) = 0.0083 to q_a(TOCestimate) = 0.0094. The goodness of fit increases especially with downstream sampling sites. This justifies the correction procedure and emphasizes the importance of an adequate estimation of tracer abundance, as described in section 3.2. The use of a one-dimensional tracer abundance estimation perpendicular to the plate boundary is potentially an oversimplification that could be improved with more field data to define variations at a smaller subcatchment resolution.

6.3. The Effect of Bed Load Modifications During Fluvial Transport

Experimentally derived rates of abrasion are generally highest for schist, lowest for sandstone, and intermediate for semischist pebbles. The abrasion rates obtained for schist are an order of magnitude higher than

abrasion rates of sandstone. Our experiments illustrated distinct evolution of abrasion rates for different rock types, and their change with progressive development of pebble rounding and preselection of stronger pebbles (see Figure 6).

In the model we have tested the same erosion functions, once including, once neglecting pebble abrasion, producing sand particles. The effect of adding bed load modification to the model had a minor impact on the best fitting erosion function. There are several potential explanations for this surprising result. First, sandstone, the least efficiently abrading bedrock lithology is hardly present in the Whataroa catchment (see Figure 1 and 8b). Pebble abrasion rates of the two dominating rock types semischist and schist are less contrasting. This reduces the effect of bed load modifications on a downstream detrital sand sample. Second, schist bedrock terranes are generally situated in the downstream part of the catchment, semischist, and sandstone bedrock terranes in the upper subcatchments toward the main divide. Consequently, in a larger downstream catchment such as wat10, semischist, and sandstone pebbles travel much longer (producing more sand particles on their way) than schist pebbles before they reach the sampling site. This is partly counterbalancing the effect of differential abrasion rates being highest for schist. In contrast, in subcatchments smaller than wat1 or wat14, the transport distances are generally too short for bed load modification to become the dominant sand particle producing process. In this case, sediment content rather reflects inheritance from hillslope supply. However, as spectacularly shown in abrasion experiments, bed load modifications may have a significant impact on provenance studies in another setting [*Attal and Lavé*, 2006].

6.4. The Effect of Sediment Supply Granulometry

The model considers the impact of sediment input properties. Sensitivity analysis suggests that the initial granulometry can be equally important as bed load modification, especially in smaller subcatchments that are associated with shorter traveled distances L_t. The larger the contribution to total sand population from one of these two processes, the weaker the effect of the other. With increasing traveled distance L_t, the effect of sediment supply granulometry is gradually overprinted by the production of particles due to pebble abrasion. Actual sediment supply granulometry has yet to be defined within the Southern Alps and is a worthy target for future field studies.

6.5. Spatial Variations of Erosion Intensity

The model calculates *T* signals, using reasonable input parameter values for bed load modification, sediment supply, and tracer abundance. When assuming equal sediment supply from each unit area, uniform erosion intensity is implied. Sampling sites lowermost in the catchment (wat10, wat12, and wat18) were systematically underrepresented by the model predictions for *T* in the range of 450°C to 550°C. As a consequence, we tested a range of large-scale erosion intensity functions (see Figure 10 for some examples) in order to derive an erosion function that best fits the field data. The goodness of fit q_a can be improved by superimposing a Gaussian erosion function maximized 10 km away from the Alpine Fault, and a mean peak width of 11 km. This is in good agreement with the pattern of rainfall intensity across the Southern Alps, which reaches a maximum in similar position [*Griffiths and McSaveney*, 1983; *Woods et al.*, 2006]. The erosion function also closely matches the pattern of short-term (contemporary) deformation measured by continuous and semicontinuous GPS stations across the Southern Alps 50 km to the southwest of Whataroa [*Beavan et al.*, 2010]. Here maximum vertical (uplift) rates occur toward the Main Divide, 10–25 km west of the Alpine Fault. The contemporary strain is thought to be largely elastic deformation adjacent to the fault, locked at shallow depth during its approximately 330 years [*Berryman et al.*, 2012] interseismic period. This contrasts with the geologic rock exposures and thermochronology that indicate long-term uplift to be greatest at [*Tippett and Kamp*, 1993], or close to [*Little et al.*, 2005; *Braun et al.*, 2010] the Alpine Fault. Our results suggest the detrital sands in bed load record a pattern of erosion that may be nearer the short-term uplift (10^1–10^3 years), rather than long-term erosion (10^4–10^6 years), potentially reflecting the rate of transport of sand-sized material through the river system.

Since landslides are a prominent source of clastic sediments in this mountain belt [*Hovius et al.*, 1997; *Korup et al.*, 2004; *Allen et al.*, 2011], our results could reflect a concentration of landslides or other sediment input about 10 km away from the Alpine Fault, possibly related to the focus of ground shaking during large earthquakes. Alternatively, inhomogeneous sediment supply across the hanging wall could reflect watershed-scale variations in soil chemical denudation rate [*Larsen et al.*, 2014] or localized slope collapse associated with the withdrawal of postglacial ice [*Barrell*, 2011].

6.6. Use of RSCM-*T* in Other Settings

The new detrital analysis we present here could be applied in other orogens. First, a growing body of work has identified that fossil organic carbon is common in the exhumed sediments of various mountain belts [e.g., Taiwan, Himalaya, Andes, and elsewhere, *Blair et al.*, 2003; *Galy et al.*, 2008; *Hilton et al.*, 2010; *Clark et al.*, 2013]. Second, the metamorphic gradients in these orogens may develop parallel to river networks and offer the possibility of tracking sediment inputs at a good spatial resolution.

7. Conclusions

This study first demonstrates that Raman spectroscopy on Carbonaceous Material can provide a useful tool to perform a statistical provenance analysis, as it combines fast data collection and treatment with a simple sampling method. In terranes where there is differential uplift and exhumation of metamorphosed sedimentary rocks, such as the Southern Alps of New Zealand, this method enables the provenance of detrital sediment in the catchment to be mapped. Clear systematic differences in RSCM-*T* distribution occur in detrital sediment samples from different subcatchments, reflecting differences in the source rocks and evolution of the distribution with travel distance, highlighting the potential of the technique.

Second, we assessed the processes that may control the shape of RSCM-*T* distributions: (1) tracer concentration in the bedrock that produces sediment, (2) spatial variations in erosion, (3) bed load modifications during fluvial transport, and (4) grain size distribution of sediment supplied to the river system. By quantifying these in the laboratory and integrating them into a simple model, we ultimately demonstrate that both spatial variations in tracer concentration and erosion have a primary control on the RSCM-*T* distributions measured on detrital sands. This observation might be important for provenance studies in general. It also implies that sand specimens are, to a first order, good proxies for detecting spatial variations in erosion, but should not be analyzed without measuring the bedrock concentration of the target mineral. Furthermore, bed load modification and grain size distribution of sediment supplied to the river can generally have a significant impact on any multilithological provenance study. In the specific case of the Whataroa catchment the effects were less pronounced because (1) contrasts in abrasion rates were not sufficiently large, (2) of the presence of relatively weak schist in the downstream part of the catchment, and (3) of the relatively small catchment scale. In another setting these factors may play a more important role.

Finally, a best fit to the data is found by applying a Gaussian erosion function that is maximized 10 km away from the Alpine Fault. The erosion recorded by detrital sands is not highest near the Alpine Fault, as might be expected from long-term metamorphic rock exhumation and thermochronologic ages, but more closely reflects the pattern of short-term (contemporary) uplift and/or patterns of rainfall. Possible explanations for inhomogeneous sediment supply, with concentrations distributed farther southeast in the hanging wall, include earthquake-induced landslides or slope collapse associated with postglacial ice withdrawal.

Appendix A: Abrasion Experiment Setup and Bedrock RSCM-*T* Data

A1. Experimental Setup

The water-circulating device generates a continuous, turbulent water flow in an annular channel, in which rock clasts mostly move in saltation. Water that contains the suspension load leaves the system through a central circular overflow. Suspended particles greater than 0.5 mm are retained by a square mesh sieve. Overflow and particles smaller than 0.5 mm fall into a large tank below the flume from where water and the finest particles are recirculated. Water discharge was set at 329 to 340 m^3h^{-1} during the experiment, developing a vortex as a result of centrifugal forces. The mean fluid velocity $U_{fl} = 2.2\ m\ s^{-1}$ and mean pebble velocity $U_p = 1.5\ m\ s^{-1}$ can be estimated as a function of vortex height dZ [*Attal and Lavé*, 2009]. The mean traveled distance of a pebble L_t can be calculated as follows:

$$L_t = U_p t \tag{A1}$$

where t is the time of pebble motion during the experiment. The experimental setup produced similar hydrodynamic conditions to those found in rivers of the western Southern Alps. The experimental fluid velocities correspond approximately to those measured in Whataroa and other nearby rivers such as Hokitika during flood conditions (www.wcrc.govt.nz).

Sediment input comprised clasts of 40 to 120 mm diameter D (defined by the size of square mesh sieves = close to the b axis length of the clasts), having a total weight of between 29 and 48 kg. The flume floor was covered

with sufficient pebbles (more than 30 to 70%) so that the abrasion rate would be independent of sediment input [*Attal and Lavé*, 2009]. The time of pebble motion *t* varied between 25 and 52 min, equating to travel distances of 2 to 5 km, respectively.

A2. Further Details on Abrasion Experiments

For experiments in zone I, 60 kg fresh angular clasts of schist, semischist, and sandstone were sampled from young talus deposits. Clasts larger than 120 mm diameter were cut using a rock saw. No obvious weathering rind was observed on the rock samples. Independent experiments were carried out for each rock lithology (EN1, EN3, and EN5) that simulate early modification of bed load in the first 5 km of fluvial transport (based on pebble velocity and experiment time).

For experiments representing zone II, we reused (then subangular) clasts larger than 40 mm from the first series of experiments, added some rounded pebbles of schist, semischist, and sandstone to ensure the flume floor was covered sufficiently, and run separate experiments for each lithology (EN2, EN4, and EN6). The experiments approximate fluvial modification from 5 to 15 km.

For the experiment in zone III, well-rounded pebbles of schist, semischist, sandstone and a small number of ultramafic pebbles (to represent lithologies in the Pacific Plate hanging wall of the Alpine Fault) and granitic pebbles (representing dominantly plutonic rocks in the Australian Plate/footwall of the Alpine Fault) were collected from gravel bars in the lower Whataroa and nearby rivers. The different lithologies were abraded together in a single experiment (EN7), thought to replicate conditions from 15 km onward.

For all runs, clasts and pebbles were first washed, left in water for a while, then weighed and photographed in three diameter classes (40 to 60 mm, 60 to 80 mm, and 80 to 120 mm) and regularly distributed on the channel floor, before injecting water. Run time *t* was recorded from the time pebble motion started until they came to rest. Vortex height d*Z* was measured twice during the experiment to estimate pebble velocity.

After each run, particles larger than 0.5 mm were collected and sieved. A standard drying and sieving procedure was applied before weighing the grain size fractions, reducing the empirical error to less than 5% [*Attal and Lavé*, 2009]. Sampling of abrasion products finer than 0.5 mm required a minimum settling time of 12 h and a complicated procedure, so were sampled after every second experiment, or before a change of input lithology, to expedite the experiments.

For the mixed lithology experiment EN7 a specific sampling procedure was necessary as it is not possible to identify the source lithology of small-sized grains. In this experiment products of abrasion were manually identified, separated, and weighted for each lithology down to a grain diameter of 5 mm. We then used RSCM-*T* to depict the proportion of sand-sized products derived from sandstone, semischist, and schist. Relative abundance was calculated with help of the RSCM-*T* bounds $T_{sst/ss}$ = 356°C and $T_{ss/sch}$ = 492°C (Figure 3), including a correction factor for TOC variations of the three rock types of interest.

Acknowledgments

The data for this paper are available by contacting the corresponding author. Robert Sparkes is thanked for providing the peak fitting code, Men-Andrin Meier for his help with MATLAB scripting, Marc-Andri Riedi for his support in the field, and Stefanie Wirth for her assistance with the total organic content measurements. The authors thank Kathleen Marsaglia for constructive comments and enthusiasm. Constructive reviews and helpful comments were provided by Bryn Hubbard, Amy East, Bob Hilton, Uwe Altenberger, Alexander Densmore, Amy Draut, Eduardo Garzanti, and Salvatore Critelli. Olivier Beyssac acknowledges funding from Ville de Paris (Emergence program) and Sorbonne Universités (PER-SU program).

References

Allen, S. K., S. C. Cox, and I. F. Owens (2011), Rock avalanches and other landslides in the central Southern Alps of New Zealand: A regional study considering possible climate change impacts, *Landslides*, *8*(1), 33–48, doi:10.1007/s10346-010-0222-z.

Attal, M., and J. Lavé (2006), Changes of bedload characteristics along the Marsyandi River (central Nepal): Implications for understanding hillslope sediment supply, sediment load evolution along fluvial networks, and denudation in active orogenic belts, in *Tectonics, Climate, and Landscape Evolution*, vol. 398, edited by S. D. Willett et al., pp. 143–171, Geol. Soc. of Am., Boulder, Colo., doi:10.1130/2006.2398(09).

Attal, M., and J. Lavé (2009), Pebble abrasion during fluvial transport: Experimental results and implications for the evolution of the sediment load along rivers, *J. Geophys. Res.*, *114*, F04023, doi:10.1029/2009JF001328.

Attal, M., J. Lavé, and J. Masson (2006), New facility to study river abrasion processes, *J. Hydraul. Eng.*, *132*, 624–628, doi:10.1061/(ASCE)0733-9429(2006)132:6(624).

Barrell, D. (2011), Quaternary glaciers of New Zealand, in *Quaternary Glaciations—Extent and Chronology: A closer look*, vol. 15, edited by J. Ehlers, P. L. Gibbard, and P. D. Hughes, pp. 1047–1064, Elsevier, Amsterdam., doi:10.1016/B978-0-444-53447-7.00075-1.

Batt, G., J. Braun, B. Kohn, and I. McDougall (2000), Thermochronological analysis of the dynamics of the Southern Alps, New Zealand, *Geol. Soc. Am. Bull.*, *112*(2), 250–266, doi:10.1130/0016-7606(2000)112<250:TAOTDO>2.0.CO;2.

Beavan, J., P. Denys, M. Denham, B. Hager, T. Herring, and P. Molnar (2010), Distribution of present-day vertical deformation across the Southern Alps, New Zealand, from 10 years of GPS data, *Geophys. Res. Lett.*, *37*, L16305, doi:10.1029/2010GL044165.

Berryman, K., A. Cooper, R. Norris, P. Villamor, R. Sutherland, T. Wright, E. Schermer, R. Langridge, and G. Biasi (2012), Late Holocene rupture history of the Alpine Fault in South Westland, New Zealand, *Bull. Seismol. Soc. Am.*, *102*(2), 620–638, doi:10.1785/0120110177.

Beyssac, O., and M. Lazzeri (2012), Application of Raman spectroscopy to the study of graphitic carbons in the Earth Sciences, in *Applications of Raman Spectroscopy to Earth Sciences and Cultural Heritage, Eur. Mineral. Union Notes in Mineral.*, vol. 12, edited by J. Dubessy, M.-C. Caumon, and F. Rull, pp. 413–452, Eur. Mineral. Union and Mineral. Union, Great Britain and Ireland.

Beyssac, O., C. Chopin, and J. Rouzaud (2002), Raman spectra of carbonaceous material in metasediments: A new geothermometer, *J. Metamorph. Geol.*, *20*(9), 19–31, doi:10.1046/j.1525-1314.2002.00408.x.

Blair, N. E., E. L. Leithold, S. T. Ford, K. A. Peeler, J. C. Holmes, and D. W. Perkey (2003), The persistence of memory: The fate of ancient sedimentary organic carbon in a modern sedimentary system, *Geochim. Cosmochim. Acta*, *67*(1), 63–73, doi:10.1016/S0016-7037(02)01043-8.

Bouchez, J., O. Beyssac, V. Galy, J. Gaillardet, C. France-Lanord, L. Maurice, and P. Moreira-Turcq (2010), Oxidation of petrogenic organic carbon in the Amazon floodplain as a source of atmospheric CO_2, *Geology*, *38*(3), 255–258, doi:10.1130/G30608.1.

Bouchez, J., J. Gaillardet, C. France-Lanord, L. Maurice, and P. Dutra-Maia (2011), Grain size control of river suspended sediment geochemistry: Clues from Amazon River depth profiles, *Geochem. Geophys. Geosyst.*, *12*, Q03008, doi:10.1029/2010GC003380.

Bradley, W. (1970), Effect of weathering on abrasion of granitic gravel, Colorado River (Texas), *Geol. Soc. Am. Bull.*, *81*(1), 61–80, doi:10.1130/0016-7606(1970)81[61:EOWOAO]2.0.CO;2.

Bradley, W., R. Fahnestock, and E. Rowekamp (1972), Coarse sediment transport by flood flows on Knik River, Alaska, *Geol. Soc. Am. Bull.*, *83*(5), 1261–1284, doi:10.1130/0016-7606(1972)83[1261:CSTBFF]2.0.CO;2.

Braun, J., F. Herman, and G. Batt (2010), Kinematic strain localization, *Earth Planet. Sci. Lett.*, *300*(3), 197–204, doi:10.1016/j.epsl.2010.08.018.

Brewer, P. (1991), Sediment reduction processes in natural rivers, Unpublished PhD thesis, Univ. College of Wales, Aberystwyth.

Brewer, P., and J. Lewin (1993), In-transport modification of alluvial sediment: Field evidence and laboratory experiments, *Alluvial Sediment.*, *17*, 23–35, doi:10.1002/9781444303995.ch3.

Clark, K., R. Hilton, A. West, Y. Malhi, D. Gröcke, C. Bryant, P. Ascough, A. Robles Caceres, and M. New (2013), New views on "old" carbon in the Amazon River: Insight from the source of organic carbon eroded from the Peruvian Andes, *Geochem. Geophys. Geosyst.*, *14*, 1644–1659, doi:10.1002/ggge.20122.

Cox, S. C., and D. J. A. Barrell (2007), *Geology of the Aoraki Area*, Inst. of Geol. and Nuclear Sci. 1:250,000 Geol. Map 15, GNS Sci., Lower Hutt., 71 pages + 1 Folded Map.

Cox, S. C., and L. Nibourel (2015), Bedload composition, transport and modification in rivers of Westland, New Zealand, with implications for the distribution of alluvial pounamu (jade), *N. Z. J. Geol. Geophys.*, *58*(2), 154–175, doi:10.1080/00288306.2015.1025799.

Cox, S. C., and R. Sutherland (2007), Regional geological framework of South Island, New Zealand, and its significance for understanding the active plate boundary, in *A Continental Plate Boundary: Tectonics at South Island, New Zealand*, vol. 175, edited by D. Okaya, T. Stern, and F. Davey, pp. 19–46, AGU, Washington, D. C., doi:10.1029/175GM03.

Cox, S. C., M. W. Stirling, F. Herman, M. Gerstenberger, and J. Ristau (2012), Potentially active faults in the rapidly eroding landscape adjacent to the Alpine Fault, central Southern Alps, New Zealand, *Tectonics*, *31*, TC2011, doi:10.1029/2011TC003038.

Dickinson, W. R. (1988), Provenance and sediment dispersal in relation to paleotectonics and paleogeography of sedimentary basins, in *New Perspectives in Basin Analysis, Part I*, edited by K. L. Kleinspehn and C. Paola, pp. 3–25, Springer, New York., doi:10.1007/978-1-4612-3788-4_1.

Dickinson, W. R. (2008), Impact of differential zircon fertility of granitoid basement rocks in North America on age populations of detrital zircons and implications for granite petrogenesis, *Earth Planet. Sci. Lett.*, *275*(1), 80–92, doi:10.1016/j.epsl.2008.08.003.

Engleman, E. E., L. L. Jackson, and D. R. Norton (1985), Determination of carbonate carbon in geological materials by coulometric titration, *Chem. Geol.*, *53*(1), 125–128, doi:10.1016/0009-2541(85)90025-7.

Galy, A., and C. France-Lanord (2001), Higher erosion rates in the Himalaya: Geochemical constraints on riverine fluxes, *Geology*, *29*(1), 23–26, doi:10.1130/0091-7613(2001)029<0023:HERITH>2.0.CO;2.

Galy, V., O. Beyssac, C. France-Lanord, and T. Eglinton (2008), Recycling of graphite during Himalayan erosion: A geological stabilization of carbon in the crust, *Science*, *322*(5903), 943–945, doi:10.1126/science.1161408.

Galy, V., C. France-Lanord, B. Peucker-Ehrenbrink, and P. Huyghe (2010), Sr–Nd–Os evidence for a stable erosion regime in the Himalaya during the past 12Myr, *Earth Planet. Sci. Lett.*, *290*(3), 474–480, doi:10.1016/j.epsl.2010.01.004.

Garzanti, E., and G. Vezzoli (2003), A classification of metamorphic grains in sands based on their composition and grade, *J. Sediment. Res.*, *73*(5), 830–837, doi:10.1306/012203730830.

Garzanti, E., G. Vezzoli, S. Andò, J. Lavé, M. Attal, C. France-Lanord, and P. DeCelles (2007), Quantifying sand provenance and erosion (Marsyandi River, Nepal Himalaya), *Earth Planet. Sci. Lett.*, *258*(3), 500–515, doi:10.1016/j.epsl.2007.04.010.

Gregory, H. E. (1915), Note on the shape of pebbles, *Am. J. Sci.*, *231*, 300–304.

Griffiths, G., and M. McSaveney (1983), Hydrology of a basin with extreme rainfalls—Cropp River, New Zealand, *N. Z. J. Sci.*, *26*(3), 293–306.

Herman, F., and J. Braun (2006), Fluvial response to horizontal shortening and glaciations: A study in the Southern Alps of New Zealand, *J. Geophys. Res.*, *111*, F01008, doi:10.1029/2004JF000248.

Herman, F., J. Braun, and W. Dunlap (2007), Tectonomorphic scenarios in the Southern Alps of New Zealand, *J. Geophys. Res.*, *112*, B04201, doi:10.1029/2004JB003472.

Herman, F., S. Cox, and P. Kamp (2009), Low-temperature thermochronology and thermokinematic modeling of deformation, exhumation, and development of topography in the central Southern Alps, New Zealand, *Tectonics*, *28*, TC5011, doi:10.1029/2008TC002367.

Herman, F., E. Rhodes, J. Braun, and L. Heiniger (2010), Uniform erosion rates and relief amplitude during glacial cycles in the Southern Alps of New Zealand, as revealed from OSL-thermochronology, *Earth Planet. Sci. Lett.*, *297*(1–2), 183–189, doi:10.1016/j.epsl.2010.06.019.

Hilton, R. G., A. Galy, and N. Hovius (2008), Riverine particulate organic carbon from an active mountain belt: Importance of landslides, *Global Biogeochem. Cycles*, *22*, GB1017, doi:10.1029/2006GB002905.

Hilton, R. G., A. Galy, N. Hovius, M.-J. Horng, and H. Chen (2010), The isotopic composition of particulate organic carbon in mountain rivers of Taiwan, *Geochim. Cosmochim. Acta*, *74*(11), GB1017, doi:10.1016/j.gca.2010.03.004.

Hilton, R. G., A. Galy, N. Hovius, M.-J. Horng, and H. Chen (2011), Efficient transport of fossil organic carbon to the ocean by steep mountain rivers: An orogenic carbon sequestration mechanism, *Geology*, *39*(1), 71–74, doi:10.1130/G31352.1.

Hilton, R. G., J. Gaillardet, D. Calmels, and J. -L. Birck (2014), Geological respiration of a mountain belt revealed by the trace element rhenium, *Earth Planet. Sci. Lett.*, *403*, 27–36, doi:10.1016/j.epsl.2014.06.021.

Hovius, N., C. P. Stark, and P. A. Allen (1997), Sediment flux from a mountain belt derived by landslide mapping, *Geology*, *25*(3), 231–234, doi:10.1130/0091-7613(1997)025<0231:SFFAMB>2.3.CO;2.

Huntington, K. W., and K. Hodges (2006), A comparative study of detrital mineral and bedrock age-elevation methods for estimating erosion rates, *J. Geophys. Res.*, *111*, F03011, doi:10.1029/2005JF000454.

Jacobson, A. D., J. D. Blum, C. P. Chamberlain, D. Craw, and P. O. Koons (2003), Climatic and tectonic controls on chemical weathering in the New Zealand Southern Alps, *Geochim. Cosmochim. Acta*, *67*(1), 29–46, doi:10.1016/S0016-7037(02)01053-0.

Kleffmann, S., F. Davey, A. Melhuish, D. Okaya, T. Stern, and SIGHT Team (1998), Crustal structure in the central South Island, New Zealand, from the Lake Pukaki seismic experiment, *N. Z. J. Geol. Geophys.*, *41*(1), 39–49, doi:10.1080/00288306.1998.9514789.

Korup, O., M. J. McSaveney, and T. R. Davies (2004), Sediment generation and delivery from large historic landslides in the Southern Alps, New Zealand, *Geomorphology*, *61*(1), 189–207, doi:10.1016/j.geomorph.2004.01.001.

Krumbein, W. (1941), The effects of abrasion on the size, shape and roundness of rock fragments, *J. Geol.*, *49*(5), 482–520. [Available at http://www.jstor.org/stable/30069332.]
Krumbein, W. (1942), Flood deposits of Arroyo Seco, Los Angeles County, California, *Geol. Soc. Am. Bull.*, *53*(9), 1355–1402.
Kuenen, P. (1956), Experimental abrasion of pebbles: 2. Rolling by current, *J. Geol.*, *64*(4), 336–368. [Available at http://www.jstor.org/stable/30056065.]
Lahfid, A., O. Beyssac, E. Deville, F. Negro, C. Chopin, and B. Goffé (2010), Evolution of the Raman spectrum of carbonaceous material in low-grade metasediments of the Glarus Alps (Switzerland), *Terra Nova*, *22*(5), 354–360, doi:10.1111/j.1365-3121.2010.00956.x.
Larsen, I. J., P. C. Almond, A. Eger, J. O. Stone, D. R. Montgomery, and B. Malcolm (2014), Rapid soil production and weathering in the Southern Alps, New Zealand, *Science*, *343*(6171), 637–640, doi:10.1126/science.1244908.
Little, T., R. Holcombe, and B. Ilg (2002), Kinematics of oblique collision and ramping inferred from microstructures and strain in middle crustal rocks, central Southern Alps, New Zealand, *J. Struct. Geol.*, *24*(1), 219–239, doi:10.1016/S0191-8141(01)00060-8.
Little, T. A., S. Cox, J. K. Vry, and G. Batt (2005), Variations in exhumation level and uplift rate along the obliqu-slip Alpine Fault, central Southern Alps, New Zealand, *Geol. Soc. Am. Bull.*, *117*(5–6), 707–723, doi:10.1130/B25500.1.
Ludwig, R. (1874), *Geologische Bilder aus Italien*, Bulletin de la Société Imperiale des Naturalistes de Moscou, Moscou.
Malusà, M. G., M. Zattin, S. Andò, E. Garzanti, and G. Vezzoli (2009), Focused erosion in the Alps constrained by fission-track ages on detrital apatites, *Geol. Soc. London Spec. Publ.*, *324*(1), 141–152, doi:10.1144/SP324.11.
Marshall, P. (1927), The wearing of beach gravels, *Trans. R. Soc. N. Z.*, *58*, 507–532.
Marshall, P. (1929), *Beach Gravels and Sands*, 324–365, vol. 60.
Massey, F. (1951), The Kolmogorov-Smirnov test for goodness of fit, *J. Am. Stat. Assoc.*, *46*(253), 68–78, doi:10.1080/01621459.1951.10500769.
McPhillips, D., and M. T. Brandon (2010), Using tracer thermochronology to measure modern relief change in the Sierra Nevada, California, *Earth Planet. Sci. Lett.*, *296*(3), 373–383, doi:10.1016/j.epsl.2010.05.022.
McSaveney, M. (2002), Recent rockfalls and rock avalanches in Mount Cook National Park, New Zealand, *Catastrophic landslides*, *15*, 35–70, doi:10.1130/REG15-p35.
Moecher, D. P., and S. D. Samson (2006), Differential zircon fertility of source terranes and natural bias in the detrital zircon record: Implications for sedimentary provenance analysis, *Earth Planet. Sci. Lett.*, *247*(3), 252–266, doi:10.1016/j.epsl.2006.04.035.
Norris, R. J., and A. F. Cooper (1995), Origin of small-scale segmentation and transpressional thrusting along the Alpine Fault, New Zealand, *Geol. Soc. Am. Bull.*, *107*(2), 231–240, doi:10.1130/0016-7606(1995)107<0231:OOSSSA>2.3.CO;2.
Parker, G. (1991), Selective sorting and abrasion of river gravel. II: Applications, *J. Hydraul. Eng.*, *117*(2), 150–171, doi:10.1061/(ASCE)0733-9429(1991)117:2(131).
Pearce, T. (1971), Short distance fluvial rounding of volcanic detritus, *J. Sediment. Res.*, *41*(4), 1069–1072, doi:10.1306/74D72400-2B21-11D7-8648000102C1865D.
Petsch, S., R. Berner, and T. Eglinton (2000), A field study of the chemical weathering of ancient sedimentary organic matter, *Org. Geochem.*, *31*(5), 475–487, doi:10.1016/S0146-6380(00)00014-0.
Pierson-Wickmann, A.-C., L. Reisberg, and C. France-Lanord (2002), Impure marbles of the Lesser Himalaya: Another source of continental radiogenic osmium, *Earth Planet. Sci. Lett.*, *204*(1), 252–266, doi:10.1016/S0012-821X(02)00962-7.
Scheingross, J. S., F. Brun, D. Y. Lo, K. Omerdin, and M. P. Lamb (2014), Experimental evidence for fluvial bedrock incision by suspended and bedload sediment, *Geology*, *42*(6), 523–526, doi:10.1130/G35432.1.
Schmeeckle, M. W., J. M. Nelson, J. Pitlick, and J. P. Bennett (2001), Interparticle collision of natural sediment grains in water, *Water Resour. Res.*, *37*(9), 2377–2391, doi:10.1029/2001WR00053.
Sibson, R., S. White, and B. Atkinson (1981), Structure and distribution of fault rocks in the Alpine Fault Zone, New Zealand, *Geol. Soc. Spec. Pub.*, *9*(1), 197–210, doi:10.1144/GSL.SP.1981.009.01.18.
Sparkes, R., N. Hovius, A. Galy, R. V. Kumar, and J. T. Liu (2013), Automated analysis of carbon in powdered geological and environmental samples by Raman spectroscopy, *Appl. Spectrosc.*, *67*(7), 779–788. [Available at http://www.opticsinfobase.org/as/abstract.cfm?URI=as-67-7-779.]
Stern, T., S. Kleffmann, D. Okaya, M. Scherwath, and S. Bannister (2001), Low seismic-wave speeds and enhanced fluid pressure beneath the Southern Alps of New Zealand, *Geology*, *29*(8), 679–682, doi:10.1130/0091-7613(2001)029<0679:LSWSAE>2.0.CO;2.
Sternberg, H. (1875), Untersuchungen über Längen- und Querprofile geschiebeführender Flüsse, *Z. Bauwes.*, *25*, 483–506.
Stock, G. M., T. A. Ehlers, and K. A. Farley (2006), Where does sediment come from? Quantifying catchment erosion with detrital apatite (U-Th)/He thermochronometry, *Geology*, *34*(9), 725–728, doi:10.1130/G22592.1.
Tippett, J. M., and P. J. Kamp (1993), Fission track analysis of the late Cenozoic vertical kinematics of continental Pacific crust, South Island, New Zealand, *J. Geophys. Res.*, *98*(B9), 16,119–16,148, doi:10.1029/92JB02115.
Turnbull, I., N. Mortimer, and D. Craw (2001), Textural zones in the Haast Schist—A reappraisal, *N. Z. J. Geol. Geophys.*, *44*(1), 171–183, doi:10.1080/00288306.2001.9514933.
Wentworth, C. (1919), A laboratory and field study of cobble abrasion, *J. Geol.*, *27*(7), 507–521.
Whitehouse, I. E. (1987), Geomorphology of a compressional plate boundary: Southern Alps, New Zealand, *Int. Geomorphol.*, *1*, 897–924.
Woods, R., J. Hendrikx, R. Henderson, and A. Tait (2006), Estimating mean flow of New Zealand rivers, *J. Hydrol. N. Z.*, *45*(2), 95–209. [Available at http://search.informit.com.au/documentSummary;dn=587262022948844;res=IELENG.]